



# Investigation of friction modeling on numerical Ti6Al4V cutting simulations

## Journal Article

### Author(s):

Zhang, Nanyuan ; Klippel, Hagen ; Kneubühler, Fabian; Afrasiabi, Mohamadreza; Kuffa, Michal; Wegener, Konrad

### Publication date:

2024-07-15

### Permanent link:

<https://doi.org/10.3929/ethz-b-000668561>

### Rights / license:

[Creative Commons Attribution 4.0 International](#)

### Originally published in:

International Journal of Mechanical Sciences 274, <https://doi.org/10.1016/j.ijmecsci.2024.109231>



Contents lists available at ScienceDirect

## International Journal of Mechanical Sciences

journal homepage: [www.elsevier.com/locate/ijmecsci](http://www.elsevier.com/locate/ijmecsci)

## Investigation of friction modeling on numerical Ti6Al4V cutting simulations

Nanyuan Zhang<sup>a,\*</sup>, Hagen Klippel<sup>a</sup>, Fabian Kneubühler<sup>a</sup>, Mohamadreza Afrasiabi<sup>b</sup>,  
Michal Kuffa<sup>a,b</sup>, Konrad Wegener<sup>a</sup><sup>a</sup> Institute of Machine Tools & Manufacturing, D-MAVT, ETH Zürich, Leonhardstrasse 21, Zürich, 8092, Switzerland<sup>b</sup> inspire AG, Technoparkstrasse 1, Zürich, 8005, Switzerland

## ARTICLE INFO

## Keywords:

Machining  
Simulation  
SPH  
Friction  
Contact states  
Model selection

## ABSTRACT

Friction significantly influences chip formation, thereby highlighting its modeling critical in numerical cutting simulations. Notably, issues like the underestimation of feed force in simulations are often attributed to inadequate friction models. Nevertheless, diverse conclusions in the literature regarding friction's behavior complicate the accurate implementation of this input. Additionally, the enormous number of the available friction models and their varied calibration methods introduce further debates over which aspects of friction modeling should receive more focus. These controversies and deficiencies hinder progress in further understanding friction's role in chip formation through numerical studies. Instead of proposing or calibrating new friction models, the current study, based on Ti6Al4V machining simulations, attempts to readdress the aforementioned controversies in a neutral stance by conducting sensitivity studies using a hybrid Smoothed Particle Hydrodynamics (SPH) - Finite Element Method (FEM) solver with Graphics Processing Units (GPU) acceleration, which is capable of efficiently executing high-resolution computations. The significant impact of friction particularly at the end of the tool-chip contact on the chip formation, physical contact states and process forces are highlighted. The behaviors of physical parameters including normal contact pressure, sliding velocity, and temperature-dependent friction models in the literature are also evaluated. Several aspects such as the shear flow stress limit, the relationship between friction and process forces, and the selection of different models are discussed. In conclusion, pragmatic recommendations for friction modeling and cutting simulation work are provided. On the one hand, the available complex physical parameter dependent friction models could not prove their necessity and should be approached cautiously. Instead, the constant Coulomb friction model without the shear stress limit, despite its simplicity, demonstrates effective and sufficient for a single set of metal cutting simulations. On the other hand, reliable on-site measurement techniques of the coefficient of friction (COF) at the tool-chip sliding contact area should be developed, with consideration of the contact length and the state of material flow. Combined with careful cutting edge preparation and suitable constitutive models, the overall accuracy of numerical cutting simulations including the feed force prediction is expected to be improved.

## 1. Introduction

Numerical simulation is extensively employed for investigating the machining process, aiming to enhance the understanding, predict physical quantities including temperature and forces, and optimize the design of cutting tools and process parameters. The advancement of modeling work is driven by these objectives. In this context, Arrazola et al. [1] provided a comprehensive review of machining process simulation studies. Since the quality of simulated results is highly dependent on model inputs such as material properties, constitutive equations, and friction models, many efforts have been devoted to this area, and recent advances in material and friction modeling have been reviewed

by Melkote et al. [2]. While the constitutive equation dominates the material yield behavior and thus plays a significant role in determining the chip form and the cutting force, the friction model largely impacts the magnitude of the feed force in numerical simulations. More importantly, friction modeling plays a critical role in regulating the chip sliding, the contact length and thus the thermomechanical load on the tool surface, which further determines the tool wear progression in the wear simulation, as highlighted by Lorentzon et al. [3]. Particularly, the numerically predicted feed force [4] and contact length [5] in metal cutting often lag behind the values obtained from experimental measurements, which is intuitively correlated with a lack of accurate

\* Corresponding author.

E-mail address: [zhang@iwf.mavt.ethz.ch](mailto:zhang@iwf.mavt.ethz.ch) (N. Zhang).<https://doi.org/10.1016/j.ijmecsci.2024.109231>

Received 15 January 2024; Received in revised form 25 March 2024; Accepted 25 March 2024

Available online 1 April 2024

0020-7403/© 2024 The Author(s). Published by Elsevier Ltd. This is an open access article under the CC BY license (<http://creativecommons.org/licenses/by/4.0/>).

**Nomenclature**

|   |   |
|---|---|
| $\bar{\Theta}$                          | Artificial stress   |
| $\alpha$                                | Clearance angle of cutting tool   |
| $\beta_{fri}$                           | Frictional heat partition coefficient for the cutting tool at the contact |
| $\chi$                                  | Taylor–Quinney coefficient  |
| $\eta$                                  | Proportion of frictional energy converted into heat                       |
| $\gamma$                                | Rake angle of cutting tool  |
| $\bar{\mu}$                             | Mean frictional coefficient   |
| $\mu$                                   | Coefficient of friction (COF)   |
| $\mu_{app}$                             | Apparent coefficient of friction  |
| $\mu_{eff}$                             | Effective local coefficient of friction in simulation                     |
| $\nu$                                   | Poisson ratio   |
| $\rho$                                  | Density   |
| $\underline{\underline{\sigma}}$        | Cauchy stress tensor  |
| $\underline{\underline{\sigma}}_y^{JC}$ | Johnson–Cook flow stress  |
| $\underline{\sigma}_n$                  | Normal contact stress   |
| $\underline{\tau}_f$                    | Frictional or tangential contact stress                                   |
| $\bar{\tau}$                            | Shear flow stress   |
| $\bar{\epsilon}_{pl}$                   | Equivalent plastic strain in Johnson–Cook model                           |
| $\dot{\bar{\epsilon}}_0$                | Reference strain rate in Johnson–Cook model                               |
| $\dot{\bar{\epsilon}}_{pl}$             | Equivalent plastic strain rate in Johnson–Cook model                      |
| $A, B, C$                               | Material constants in Johnson–Cook model                                  |
| $c$                                     | Speed of sound  |
| $c_p$                                   | Specific heat   |
| $c_1, c_2, \dots$                       | Constants in friction models  |
| $E$                                     | Young's modulus   |
| $\underline{e}_{ij}$                    | Unit vector between particle $i$ and $j$                                  |
| $\underline{f}_{-cont}$                 | Normal contact force  |
| $\underline{f}_{-fri}$                  | Frictional force  |
| $F_c$                                   | Specific cutting force in orthogonal cutting                              |
| $F_f$                                   | Specific feed force in orthogonal cutting                                 |
| $h$                                     | Uncut chip thickness  |
| $h_c$                                   | Thermal contact conductance coefficient                                   |
| $h_{ch,max}$                            | Maximum chip thickness  |
| $h_{ch,min}$                            | Minimum chip thickness  |
| $h_s$                                   | Smoothing length in SPH method  |
| $i, j$                                  | Particle index in SPH   |
| $J_2$                                   | Second variant of deviatoric stress tensor                                |
| $\bar{k}_f$                             | Flow stress   |
| $k$                                     | Heat conductivity   |
| $\kappa$                                | Interface stiffness constant  |
| $l_c$                                   | Contact length  |
| $M$                                     | Mass  |
| $m_p$                                   | Particle mass   |
| $\underline{n}$                         | Normal vector on the tool-workpiece interface                             |
| $n, m$                                  | Material constants in Johnson–Cook model                                  |
| $n_c$                                   | Dimension dependent constant in SPH                                       |

|                   |  |
|-------------------|--|
| $\Omega$          | Whole computational domain                             |
| $\underline{P}$   | Momentum vector  |
| $p$               | Particle   |
| $\partial\Omega$  | Boundaries for computational domain                    |
| $\Pi_{ij}$        | Artificial viscosity                                   |
| $\dot{q}$         | Power source term                                      |
| $q$               | Normalized distance in SPH method                      |
| $r_n$             | Cutting edge radius                                    |
| $R_t$             | Thermal conductance resistance                         |
| $\underline{S}$   | Deviatoric stress tensor                               |
| $\Delta t$        | Time step  |
| $T$               | Temperature  |
| $T_0$             | Initial temperature                                    |
| $T_m$             | Melting temperature in Johnson–Cook model              |
| $T_r$             | Reference temperature in Johnson–Cook model            |
| $\underline{v}$   | Velocity vector  |
| $\underline{v}_s$ | Relative sliding velocity at the contact               |
| $v_c$             | Cutting speed  |
| $W, W_c$          | Smoothing kernel, cubic smoothing kernel in SPH method |
| $\Delta x$        | Particle distance                                      |
| $\underline{x}$   | Position vector  |

techniques. Furthermore, exploring the effects of friction modeling on numerical cutting simulation results is essential for gaining a better understanding of the role of friction in chip formation and determining the most significant factors to consider when developing friction models.

### 1.1. Available friction models for metal cutting problem

The classic Coulomb or Coulomb-Amonton friction law implies that the frictional stress  $\tau_f$  is proportional to the normal stress  $\sigma_n$  at the contact, and such a proportion is independent of the contact area as well as the sliding velocity:

$$\tau_f = \mu\sigma_n, \quad (1)$$

in which a constant coefficient of friction is assumed for the entire contact area. In light of the observed chip sticking phenomenon near the cutting edge, Zorev [6] proposed to limit the frictional stress to the shear flow stress of the material in this region. The author introduced the concept of dividing the tool-chip contact into two distinct regions: the sticking zone and the sliding zone. While the determination of the frictional stress in the sliding zone is in accordance with Eq. (1), a constant shear flow stress is employed as the frictional stress in the sticking region:

$$\begin{cases} \tau_f = \bar{\tau} & \text{in sticking zone,} \\ \tau_f = \mu\sigma_n & \text{in sliding zone,} \end{cases} \quad (2)$$

where  $\bar{\tau} = \bar{k}_f / \sqrt{3}$  is the shear flow stress of the material when the von Mises yield criterion is considered, and  $\bar{k}_f$  represents the material flow stress. Although the original concept by Zorev prescribed the stick and slide zones specifically on the rake face, many contemporary machining simulation studies implement the limitation of frictional stress by the shear flow stress across the entire contact region without predefining two distinct zones. As a result, the formulation of the friction model is modified accordingly as

$$\tau_f = \min(\bar{\tau}, \mu\sigma_n). \quad (3)$$

friction modeling. To address the challenge of identifying physical parameters for the friction model, it is crucial to conduct a detailed examination of both the friction modeling methodology and measurement

Besides the Coulomb model with a constant COF value, there are various friction models available in the literature that consider the COF as a function of physical variables. Depending on the measurement technique, calibration methods, and numerical software, the COF value can either be applied uniformly to the entire tool-chip interface for a particular cutting parameter test, or can vary locally across the contact region based on the physical contact conditions. A comprehensive enumeration of available friction models used in numerical cutting simulations is referred to Liang et al. [7]. Some of the physical parameters typically considered in friction modeling include:

- Relative sliding velocity  $v_{rel}$

A concise friction model that considers  $v_{rel}$  was originally given by Zemzemi et al. [8] as

$$\mu = c_1 \cdot |v_{rel}|^{c_2}. \quad (4)$$

in which  $c_1$  and  $c_2$  are model constants that need to be identified. Several researchers, including Rech et al. [9], Smolenicki et al. [10], and Denkena et al. [11], have utilized this exponential term to fit experimentally measured COF. In their tests, the relative sliding velocity  $v_{rel}$  varied up to 300 m/min. It is frequently found in friction measurements that the COF value decreases with the increase of  $v_{rel}$  from tribometer tests, especially in the dry machining process,  $c_2$  is thus negative in Eq. (4). Lim et al. [12] proposed an explanation for this phenomenon, suggesting that the higher flash temperature and the formation of a “melt lubrication” layer could contribute to the observed effect. However, the reliability of such a trend is still uncertain. Experimental studies by Ozlu et al. [13] on non-cutting and cutting experiments indicated that the sliding friction coefficient between AISI 1050 steel or Ti6Al4V and various tool materials is almost unaffected by  $v_{rel}$ . Similarly, experimental findings by Schulze et al. [14] did not reveal a clear trend in the change of the COF with increasing  $v_{rel}$ . Moreover, the results from Meier et al. [15] even demonstrated an opposite trend, where the COF value increased with an increase in  $v_{rel}$  between Ti6Al4V and tungsten carbide materials in the range of 20 to 100 m/min.

- Normal contact pressure  $\sigma_n$

Amonton’s law, which assumes that the coefficient of friction is independent of the normal contact pressure, is generally valid when the real contact area is much smaller than the apparent contact area. However, in machining processes, particularly around the cutting edge region, the chip material comes into close contact with the cutting tool, challenging the assumption of contact pressure independence. Bonnet et al. [16] reported that in the presence of lubricants, the measured COF decreases as the contact pressure increases in the range of 330 to 1000 MPa at the Ti6Al4V-carbide interface. Egana et al. [17] and Meier et al. [15] also observed a similar trend for the same contact pair under dry sliding conditions. However, certain materials like AISI 4142 [8] do not exhibit a significant dependency of friction on contact pressure. The reason for this heterogeneity in the friction behavior of different materials is still unknown. Concerning the modeling aspect,  $\sigma_n$  is commonly incorporated into friction models along with other physical parameters such as  $v_{rel}$  and  $T$  for metal cutting simulations. One of the available models is proposed by Brocaïl et al. [18] as

$$\mu = \mu_0 \cdot \sigma_n^{c_1} \cdot |v_{rel}|^{c_2} \cdot T^{c_3}, \quad (5)$$

where  $\mu_0$ ,  $c_1$ ,  $c_2$  and  $c_3$  are model constants to be calibrated for the respective tool-workpiece pair. In fact, this model later has been modified and is more frequently used in the metal forming field [19]. A recent study from Schulze et al. [14] presented a revised form

$$\mu = \mu_0 \cdot \left(\frac{\sigma_n}{\sigma_{n0}}\right)^{c_1} \cdot \left(\frac{|v_{rel}|}{v_{rel0}}\right)^{c_2} \cdot \left(\frac{T - T_m}{T_0 - T_m}\right)^{c_3}, \quad (6)$$

in which reference values  $\sigma_{n0}$ ,  $v_{rel0}$  and  $T_0$  are introduced so that the transcendental function becomes dimensionless. The authors conducted the tribometer test between AISI 1045 and cemented carbide materials and subsequently calibrated model constants in Eq. (6).

- Temperature  $T$

The measured COF generally decreases with the increase in the testing temperature. Moufki and colleagues [20] were the first to introduce a friction law that varies with temperature employed in their analytical modeling of machining operations. In their studies, the average temperature  $\bar{T}$  on the rake face was calculated and used to fit a piecewise function for the COF value. Later on, the same authors [21] formulated the temperature dependency into a single exponential function, and the mean friction coefficient is given as

$$\bar{\mu}(T) = \mu_0 \cdot \left[1 - \left(\frac{\bar{T}}{T_m}\right)^q\right], \quad (7)$$

where  $T_m$  denotes the melting temperature of the workpiece material and  $q$  is a model constant. Puls et al. [22] revised the model by introducing a reference temperature  $T_r$  in Eq. (7):

$$\mu(T) = \mu_0 \cdot \left[1 - \left(\frac{T - T_r}{T_m - T_r}\right)^q\right]. \quad (8)$$

Rather than an averaged value, this updated model represents the COF locally at the tool-chip contact and thus is more applicable for the numerical cutting simulation. This model shares the same form as the thermal softening term in the Johnson–Cook (JC) constitutive model [23]. Unlike  $v_{rel}$  and  $\sigma_n$ , which can be directly controlled during the tribological test, the regulation of the temperature on the contact is rather challenging. Consequently, directly identifying a temperature-dependent friction law is not feasible. Instead, an inverse approach using numerical simulations is often adopted for the model calibration. Examples can be referred to Peng et al. [24] and Afrasiabi et al. [25].

It is essential to define the effective range of friction models to ensure that the physical conditions in the application scenario remain within the limits achieved during experimental measurements.

## 1.2. Measurements of friction between tool and workpiece materials

There are numerous studies in the literature that focus on measuring the friction between the workpiece and tool materials. Reviews of recent advances in experimental friction measurements for the machining process can be referred to Segebadé et al. [26] and Storchak et al. [27]. It is important to carefully evaluate the applicability of experimentally calibrated COF values and models. This requires a thorough investigation of the tribosystem that is replicated in the measurement techniques. These techniques can be categorized based on whether they measure the friction directly from the cutting process or not.

### 1.2.1. COF measurement from cutting process

The friction on the rake face of the cutting tool can be estimated directly from the machining forces using the Merchant’s law [28]. In orthogonal cutting, the so-called apparent coefficient of friction on the tool-chip contact can be determined by

$$\mu_{app} = \frac{F_c \sin(\gamma) + F_f \cos(\gamma)}{F_c \cos(\gamma) - F_f \sin(\gamma)}, \quad (9)$$

in which  $F_c$  and  $F_f$  are the cutting and feed forces,  $\gamma$  is the rake angle of the tool. Nevertheless, the ploughing around the cutting edge and the friction on the clearance face are not excluded. Another approach is using the Abracht law [29] to derive the apparent COF. By excluding

the ploughing force  $F_{pl}$  in the force terms of Eq. (9), the apparent COF is obtained by

$$\mu_{app} = \frac{(F_c - F_{pl,c}) \sin(\gamma) + (F_f - F_{pl,f}) \cos(\gamma)}{(F_c - F_{pl,c}) \cos(\gamma) - (F_f - F_{pl,f}) \sin(\gamma)}. \quad (10)$$

Wyen and Wegener [30] applied this method to calculate the apparent COF between the Ti6Al4V workpiece and uncoated cemented carbide tool. Based on the same principle,  $\mu_{app}$  can alternatively be obtained by the force variation upon the change of the uncut chip thickness  $h$  as

$$\mu_{app} = \frac{\Delta F_f(\Delta h)}{\Delta F_c(\Delta h)}. \quad (11)$$

An example is referred to Arrazola et al. [31], in which the friction between the AISI 4140 steel and the rake face of the uncoated carbide tool was identified for cutting simulations using the Finite Element Method (FEM). The authors further stated the inadequacy of using a constant Coulomb's COF in the machining simulation. Based on the principle in Eq. (11), Denkena et al. [11] recently used the digital particle image velocimetry method to identify the sliding velocity of the chip and managed to determine velocity dependent apparent friction models for AISI 4140 workpieces in contact with various coated carbide inserts.

In addition to deriving friction coefficients from orthogonal cutting conditions, there are methods that involve specially designed cutting tools to locally measure the normal and tangential stresses on the rake face. This allows for the determination of the COF value at different locations within the contact area. One popular choice is the split tool method, which was originally proposed by Kato et al. [32]. Childs [33] summarized the results obtained using the split tool method and confirmed that in the contact region where the normal contact pressure is relatively low, the measured frictional stress shows a linear relationship with the normal contact stress. This suggests that the Coulomb friction law appears to be applicable in such cases. As the contact region approaches the cutting edge, the distributions of normal and frictional stresses exhibit different behaviors depending on the workpiece material. In the case of copper and aluminum alloys, the normal and frictional stresses show a stable level around the cutting edge [32]. However, for certain types of ferrous materials as described in [34], the normal stress increases as it gets closer to the cutting edge, while the frictional stress remains relatively constant. This discrepancy in stress variations indicates that the Coulomb friction law is no longer applicable in such situations. Interestingly, both studies [32,34] have reported that the local frictional stress can exceed the normal contact stress, resulting in a COF value greater than 1. Another recently developed method is the partially restricted contact length tool method, introduced by Ortiz-de-Zarate et al. [35]. In this method, the contact area between the tool and the chip is reduced by removing material on the tool's rake face so that the contact length is smaller than the natural one. The measured normal and frictional contact stresses between the rake face of various carbide inserts and the AISI 1045 alloy also indicate that the COF can be larger than 1 in the sliding region. Storchak et al. [27] performed a similar experiment by varying the length of the rake face of the cutting tool. The authors introduced a novel approach where they combined experimental, analytical, and numerical techniques to estimate the forces acting on the primary, secondary, and tertiary deformation zones separately. This approach enabled the determination of the COF values for the rake and clearance faces of the tool individually. Nevertheless, for the modification of the rake face, additional research is necessary to comprehend how variations in the contact area affect the stress distribution on the rake face. It should be emphasized that the COF values obtained from cutting tests may not be universally applicable, and constructing physical parameter dependent friction models based on these measurements is challenging due to difficulties in accurately identifying local contact parameters.

### 1.2.2. COF measurement from tribometer tests

Tribometer tests generally involve applying pressure and rubbing an object with certain surface curvatures, e.g., a ball or pin made of the same material as the cutting tool, against a flat work material surface. These tests, such as the pin-on-disk tribometer test, focus on the interaction between two target surfaces. For modeling the friction of the machining process, most tribometer tests aim to create an open tribosystem where the pin scratches over areas that have not been previously affected, as the cutting tool interacts with the newly generated chip and work material surface during the machining. While the objective of tribometer tests is to reproduce the tool-workpiece contact conditions in real machining, achieving a complete replication within an external tribosystem is complicated due to the following reasons:

- Physical contact conditions

Physically, the contact conditions relevant to the tribometer tests mainly include the contact pressure, sliding velocity, and temperature. To accurately replicate the contact conditions experienced during machining, the load applied on the pin should be sufficient to achieve high contact pressures, reaching several GPa. Additionally, the relative sliding speed should be compatible with the cutting speed observed in the machining process. While commercial tribometers may face challenges in reaching extreme contact conditions typical for machining, specially designed test rigs using machine tools can overcome these limitations. Several examples of such test rigs can be found in the literature [36–38]. More detailed discussions on these experimental techniques can be found in the review works by Melkote et al. [2] and Segebade et al. [26]. When it comes to controlling the temperature during tribometer tests, there are relatively few examples available in the literature. Leveille et al. [39] developed a laser-preheated tribometer and used numerical tools to estimate the temperature at the moment immediately prior to the establishment of contact. However, maintaining precise temperature control throughout the test duration is not feasible, as the temperature continues to rise during sliding due to local plastic deformation and frictional heat.

When considering the contact geometry, the pin-on-disk tribometer test, designed to resemble a Hertzian point contact, exhibits different behavior compared to the Hertzian line contact, which is more akin to the tool-workpiece interaction at the clearance face. Moreover, the contact between the tool's rake face and the generated chip presents yet another situation. The significance of these variations and their potential impacts should be acknowledged for friction measurements.

- Oxidation of material

The pin-on-disk tribometer test deviates from the tool-chip contact in the cutting process due to the presence of an oxidation layer on the work material surface. Olsson et al. [40] firstly modified the test setup and placed the test pin behind the cutting insert on the freshly machined surface to measure the friction during the turning process. However, the achieved contact pressure in their test was only around 15 MPa, which is significantly lower than the value in the cutting process. Later on, Zemzemi et al. [8], Smolenicki et al. [10] and Meier et al. [15] optimized the design of the cutting tribometer such that the applied contact pressure on the pin can reach to several GPa. However, the limitation of the cutting tribometer is that it can only provide information about the friction condition between the machined material and the clearance face of the tool. Concerning the friction at the tool-chip interface, the hardening condition of the material which will be addressed in the subsequent section might potentially restrict the applicability of results obtained from cutting tribometers.

- Hardening state of material

At the contact side of the chip where the secondary deformation zone is located, the material undergoes significant deformation

and hardening, which can lead to different frictional behavior on the rake surface compared to the clearance surface. Schulze et al. [14] demonstrated that the microhardness value at the chip's contact side shows a significant increase compared to the original material in the AISI 1045 machining process. They argued that the alteration of surface integrity can cause a change in tribological conditions, and therefore the friction measured at the surface of the base material may not accurately reflect the friction at the tool-chip interface during the cutting. A similar argument has been proposed in the study of Leveille et al. [39] as well. Consequently, a classical pin-on-disk tribometer or even the cutting tribometer cannot accurately represent the friction conditions at the tool-chip contact. While it may seem reasonable to develop a friction model that incorporates material hardness, the difficulty lies in accurately assessing the hardness of the chip's contact side during the sliding, as this value may undergo variations during the rapid cooling phase.

- Interface medium

The interface media in the tool-chip contact primarily consists of wear particles and metalworking fluid. The friction behavior at the tool-chip interface can be influenced by the quantity of particles generated due to abrasion or attrition of the tool material, which varies based on the contact pair and process parameters. The difference in wear behaviors between the pin in the tribometer test and the tool in the cutting process thus contributes to the complexities of friction modeling. Instances can be drawn from tribometer tests involving closed tribosystems, which have the capacity to introduce a higher quantity of debris into the contact region. The results from Meier et al. [15] showed a decreasing trend of the COF value as the AlTiN-coated carbide pin repeatedly slid on the same track of Ti6Al4V work material in a dry condition. However, Bonnet et al. [16] found that the COF value slightly increased as the uncoated carbide pin continued sliding on the Ti6Al4V work material in a closed tribosystem with the involvement of emulsion. Although the test conditions were not directly comparable, the contrasting results highlight the intricacies arising from different interface media. Regarding metalworking fluids, their utilization during cutting tests introduces distinct effects compared to those in tribometer tests. This divergence arises because these substances may not efficiently reach the region near the cutting edge during machining.

In summary, no single measurement technique exists that can fully capture all the factors discussed above. This lack of dependable measuring methods further compounds the challenge of selecting an appropriate friction model for numerical cutting simulations.

### 1.3. Friction modeling in numerical metal cutting simulations

The behavior of friction models in the metal cutting simulation has been investigated since the beginning of this century. Özel [41] evaluated various friction models in simulating the orthogonal cutting of low-carbon-free-cutting steel. Among the evaluated models, the one that incorporated the normal contact pressure calibrated from the split tool method demonstrated superior performance in predicting forces and chip geometry. Filice et al. [42] conducted a study in which they compared simulated cutting results of AISI 1045 using different friction models, with and without the shear flow stress limit. The authors found that the thermal field was more sensitive to the choice of friction models compared to the force results. Iqbal et al. [43] demonstrated a strong correlation between the implemented friction model and the simulated contact length in AISI 1045 cutting modeling. It is noteworthy that all the studies mentioned above highlighted the necessity of jointly considering the constitutive and friction models to enhance the cutting simulation. Arrazola and Özel [44] conducted a comprehensive study to examine the performance of the constant Coulomb friction model

and the impact of the shear flow stress limitation in simulating the machining of AISI 4340 steel. The authors obtained slightly different conclusions compared to the results from Filice et al. [42] and argued that friction modeling, especially the limitation of the shear flow stress, has a significant impact on the simulated process forces, and that the influence on the feed force is even greater. They questioned the naturalness of using the shear flow stress limitation and emphasized the importance of carefully determining the threshold value for the friction model. However, the authors reported some cases where the simulated feed force values with the shear flow stress limit were larger than those obtained with the constant Coulomb model, which is counterintuitive. Atlati et al. [45] conducted numerical simulations of aluminum alloy AA2024 machining using different COF values with a shear flow stress limited Coulomb friction model. The study showed that the formation of the build-up edge (BUE), as well as the simulated contact length, were closely linked to the applied COF value.

In the context of the friction model identification using the inverse method through numerical simulations, the typical approach involves determining parameters within the friction model while keeping a given constitutive model constant. This approach is exemplified in the work of Franchi et al. [46], where a constant Coulomb COF value was determined, and in the research by Afrasiabi et al. [25], which involved calibrating constants within a temperature-dependent friction model Eq. (8). However, it is worth noting that the friction model identified could also be compensating for shortcomings in the constitutive model, as indicated by the authors themselves. Alternatively, Klippel [47] performed calibration on both the unknowns within the constitutive model and the COF value in the constant Coulomb friction model simultaneously. Nevertheless, while the previously mentioned issue remains unsolved, the influence of friction on the simulated results becomes unclear. Particularly, when the friction model incorporates multiple physical factors outlined in Section 1.1, including temperature and sliding velocity, disentangling the influences of these separate variables becomes challenging.

Although not directly linked to the knowledge of friction modeling, it is still worth mentioning the numerical method and software used in analyzing friction modeling behaviors in metal cutting simulations. Nearly all of the studies discussed above utilized the Finite Element Method (FEM) as their numerical simulation tool. The reason behind this choice is the well-established application of FEM in thermomechanical problems and the availability of commercial software. Malakizadi et al. [48] conducted a comparison of friction models in simulating the machining of two steel materials using various commercial FEM software. Interestingly, the study found that given the same friction model, the average errors in simulated chip thickness, forces, and contact length were similar across all the tested software.

An increasing number of different approaches, especially meshless methods, are being attempted as substitutes for the FEM in modeling the chip formation process. These methods include the SPH [49–52], Discrete Element Method [53], Finite Pointset Method (FPM) [54], Particle Finite Element Method (PFEM) [55], Element-Free Galerkin Method (EFG) [56], Material Point Method (MPM) [57,58], Constrained Natural Element Method (CNEM) [59] and so on. A review of the cutting simulation using meshless methods can be referred to Markopoulos et al. [60]. In fact, one of the major advantages compared to using the FEM is to avoid the mesh related problem and improve computational efficiency. When applying meshless methods in metal cutting modeling, particles can move and interact freely without being constrained by a fixed connectivity like the material based mesh in FEM. As a result, the creation of new surfaces occurs naturally as particles separate and form distinct boundaries, which eliminates the need to predetermine the removal of material through the deletion of elements or layers in FEM modeling [61]. Despite the widespread attempts of using meshless methods in cutting simulation, the majority of these meshless modeling studies has only conceptually demonstrated their potential for simulating the metal cutting process, with comprehensive validations

still lacking. Consequently, many of these conceptual studies do not progress to further research or development, leaving a gap in the succession of practical applications. There are very few instances where other numerical techniques have been used for studying friction modeling in metal cutting. Afrasiabi et al. [25] used an in-house developed SPH software named *iwf\_mfree* to simulate the Ti6Al4V orthogonal cutting process, in which the workpiece and cutting tool were both discretized into particles spatially. The authors took advantage of GPU acceleration for conducting simulations with high resolution efficiently and inversely calibrated the constants of Eq. (8).

#### 1.4. Research gaps and present work

Friction modeling has a significant impact on multiple aspects of the cutting simulation, and selecting an appropriate friction model and precisely determining its parameters is challenging but crucial for acquiring reliable insights into the chip formation process. The enormous number of available friction models and calibration methods exists, with various researchers advocating for their approaches but without proving the necessity. This suggests research gaps in understanding the role of friction in simulations with the following items being summarized:

- The effects of restricting frictional stress by shear flow stress on simulated chip formation and process forces are not completely comprehended.
- The validity of the numerous friction models in chip formation simulations remains questionable.
- The reasons for the underestimated feed force are not well emphasized.

In fact, one of the most critical reasons is the lack of studies on friction modeling that use simulations with high spatial resolution, particularly in the secondary deformation zone. Such simulations could offer more precise depictions of the deformation gradient, thereby providing in-depth insights into the behavior of friction models in cutting simulations.

This study utilizes the SPH solver *iwf\_mfree*, a tool previously developed and extensively used in machining simulations for its ability to perform rapid computations on GPUs [25,47,62]. Building on this foundation, the SPH solver incorporates an enhanced hybrid SPH-FEM model [63], which is designed to replace the particle based tool with finite element mesh and thus can further increase the computational efficiency. The newly developed SPH-FEM cutting model has also been applied in conducting tool wear progression simulations [64]. Consequently, this hybrid model is used in the current work to explore the friction modeling in fine-resolution simulations of segmented Ti6Al4V chip formation based on the updated Lagrangian framework. The workpiece material applied here differs from the majority of friction modeling studies, which typically focus on materials that generate continuous chip forms like low to medium carbon steel or aluminum alloys. In scenarios involving continuous chip formation, it is possible to predefine the chip's geometry, enabling the use of Arbitrary Lagrangian–Eulerian (ALE) or Coupled Eulerian–Lagrangian (CEL) approaches for simulations that offer rapid, though not highly accurate for tracking the material history. Another variation due to the change of the generated chip form lies in the potential effect of the segmented chip formation on the dynamics and stability of the cutting process, as highlighted in [65]. However, addressing this aspect necessitates examining the whole machining system, which is outside the scope of the present research.

The layout of this manuscript is constructed as follows: Section 2 provides an overview of the numerical modeling approach used in the study. In Section 3, auxiliary cutting experiments are introduced. In Section 4, sensitivity analyses are performed to evaluate how different friction models influence the outcomes of chip formation simulations. The discussions in this section revolve around several key aspects,

including the correlation between friction modeling and the physical contact states, the issue of underestimating the feed force in simulations, and the implementation of the shear flow stress limit in friction modeling. Finally, Section 5 presents the conclusions of the study and suggests possible directions for future research.

## 2. Governing equations and numerical methods

The objective of this section is to provide essential information related to the involved governing equations and the related discretization relevant to the metal cutting problem. Contact modeling as well as friction models to be investigated in this study are also listed at the end of this section.

### 2.1. Modeling of orthogonal cutting simulations

Fig. 1(a) illustrates the cutting simulation model used in the study. The Ti6Al4V workpiece is discretized into SPH particles, enabling the thermomechanical analysis to accurately capture large deformations without introducing mesh-related problems. The uncoated cemented carbide WC(Co) tool is treated as a rigid but thermally conductive body and represented by FEM mesh, which allows for an efficient calculation of the temperature field. The particle distance is set to 1.44  $\mu\text{m}$  for the workpiece, which is sufficient for representing the deformation gradient in the shear band [66]. A linear triangular mesh is employed to discretize the cutting tool. The finite element mesh size varies from 2 to 120  $\mu\text{m}$  depending on the distance to the tool-chip contact. The simulation model is designed to be compatible with Graphics Processing Unit (GPU) acceleration for faster calculations. To quickly reach the steady thermal state of the modeled tool-workpiece system and thus reduce the influence of temperature change on the simulated results, the FEM tool is specified with a warm temperature profile obtained by conducting the repetitive long-distance cutting simulation of 15 mm in total with a constant COF as 0.35. The effects due to the alterations in the COF values, as examined later in the sensitivity study, can be eliminated within a short cutting distance. The benchmarks of the thermomechanical solver *iwf\_mfree* can be referred to the previous studies [63,66].

#### 2.1.1. Conservation equations

The total mass  $M$  can be written as the integration in the domain  $\Omega$ :

$$M = \int_{\Omega} \rho d\Omega, \quad (12)$$

in which  $\rho$  is the density. The mass conservation can be given as

$$\frac{DM}{Dt} = \frac{D}{Dt} \int_{\Omega} \rho(\underline{x}, t) d\Omega = 0, \quad (13)$$

where  $\underline{x}$  is the position vector. Applying the Reynolds transport theorem:

$$\begin{aligned} \frac{DM}{Dt} &= \int_{\Omega_0} \left( \frac{\partial \rho(\underline{X}, t)}{\partial t} + \rho(\underline{X}, t) \nabla \cdot \underline{v} \right) J d\Omega_0 \\ &= \int_{\Omega} \left( \frac{D\rho(\underline{x}, t)}{Dt} + \rho(\underline{x}, t) \nabla \cdot \underline{v} \right) d\Omega = 0, \end{aligned} \quad (14)$$

in which  $J$  represents the Jacobian of the deformation gradient,  $\underline{v}$  is the velocity vector,  $\underline{X}$  is the position vector in the reference domain  $\Omega_0$ . As the differential volume  $d\Omega$  is arbitrary in the control volume, the integration can be dropped. As a result, the continuity equation can be written as:

$$\frac{D\rho}{Dt} + \rho(\nabla \cdot \underline{v}) = 0. \quad (15)$$

As for the momentum conservation, it is given as

$$\frac{DP}{Dt} = \frac{D}{Dt} \int_{\Omega} \rho(\underline{x}, t) \underline{v} d\Omega = F = \int_{\Omega} \rho(\underline{x}, t) \underline{b}(\underline{x}, t) d\Omega + \int_{\partial\Omega} \underline{t} d\partial\Omega, \quad (16)$$

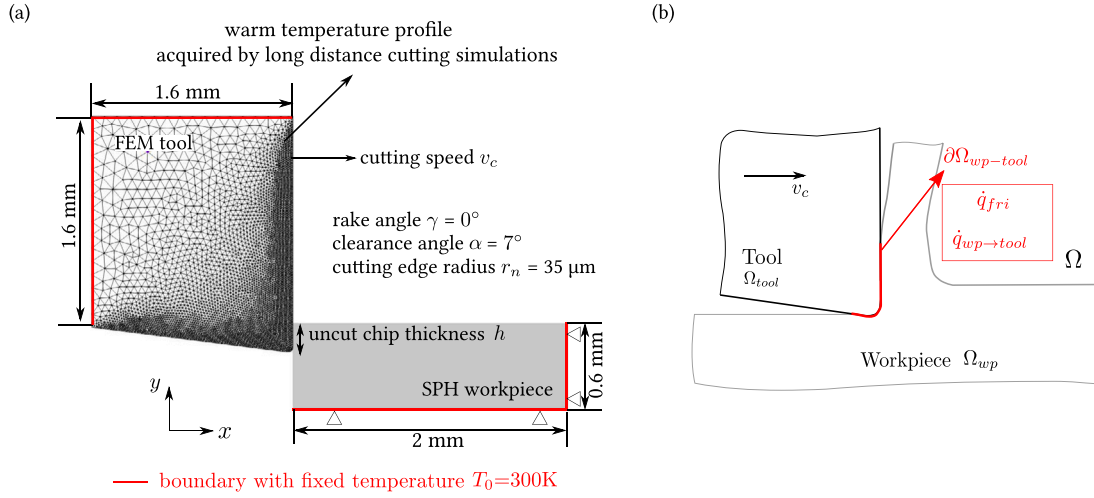


**Fig. 1.** (a) Configuration of the hybrid SPH-FEM chip formation simulation model. The represented height of the workpiece here is 0.6 mm, corresponding to the process parameter when  $h = 0.2$  mm. Generally, this height value of the workpiece is set flexibly and adjusted to be at least three times the uncut chip thickness value. (b) Illustration of the computational domain around the cutting edge, in which  $\Omega_{tool}$  and  $\Omega_{wp}$  represent the tool and workpiece domains respectively. Thermal contacts on the workpiece-tool interface  $\partial\Omega_{wp-tool}$  are treated as boundary conditions for the numerical methods.

in which  $\underline{P}$  is the momentum of the system,  $\underline{b}$  denotes the volumetric body force,  $\underline{t}$  is the traction vector acting on the surface,  $\underline{\sigma}$  is the Cauchy stress tensor. With the divergence theorem applied to the right hand side and the Reynolds transport theorem applied to the left hand side, the above equation can be written as:

$$\int_{\Omega} \rho(\underline{x}, t) \frac{D\underline{v}}{dt} d\Omega = \int_{\Omega} \rho(\underline{x}, t) \underline{b}(\underline{x}, t) d\Omega + \int_{\Omega} \nabla \cdot \underline{\sigma} d\Omega. \quad (17)$$

Thus, the momentum conservation can be expressed as:

$$\frac{D\underline{v}}{dt} = \frac{1}{\rho} \nabla \cdot \underline{\sigma} + \underline{b}. \quad (18)$$

Regarding the thermal energy, the heat conduction equation is considered:

$$\rho c_p \frac{\partial T}{\partial t} = \nabla \cdot (k \nabla T) + \dot{q}, \quad (19)$$

where  $T$  is the temperature,  $c_p$  is the specific heat,  $k$  is the heat conductivity,  $\dot{q}$  is the power source term. The heat sources consist of the dissipated energy from plastic deformation  $\dot{q}_{plast}$ , as well as the friction  $\dot{q}_{fri}$  at the sliding interface. The definitions of these two terms are expressed as follows:

$$\begin{cases} \dot{q}_{plast} = \chi \sigma_y^{JC} \dot{\bar{\epsilon}}_{pl}, \\ \dot{q}_{fri} = \eta \underline{f}_{fri} \cdot \underline{v}_{rel}, \end{cases} \quad (20)$$

in which  $\chi$  is the Taylor–Quinney coefficient [67] representing the fraction of plastic work converted into heat. This parameter is assumed as 0.9, with the remaining of the plastic energy stored in structural changes.  $\eta$  is the proportion of frictional energy converted into heat and assumed as 1, which indicates that all the frictional energy is converted into the thermal energy.  $\underline{f}_{fri}$  is the frictional force and  $\underline{v}_{rel}$  is the relative sliding velocity.

### 2.1.2. Material modeling regarding plastic deformation

A brief introduction is provided for key terms related to describing material behavior, specifically focusing on the plastic deformation of the workpiece material. The terms covered include the yield criterion, hardening law and flow rule. Other aspects in the material modeling such as the kinematics, strain and stress measures, energetic conjugates and elasticity modeling will not be discussed.

Regarding the yield surface, the von Mises yield criterion is applied in this study:

$$F(J_2) = \sqrt{3J_2} - \sigma_y = 0, \quad (21)$$

in which  $J_2$  is the second invariant of the deviatoric stress  $\underline{S}$ ,  $\sigma_y$  denotes the yield stress. In fact, the term  $\sqrt{3J_2}$  is often referred to as the equivalent stress or the von Mises stress  $\sigma_{vm}$  and serves as a criterion for the yielding of ductile materials under complex stress states.

The Johnson–Cook (JC) hardening law is implemented to define the isotropic hardening behavior of the workpiece material. The flow stress is given as:

$$\sigma_y^{JC}(\bar{\epsilon}_{pl}, \dot{\bar{\epsilon}}_{pl}, T) = [A + B(\bar{\epsilon}_{pl})^n] \left[ 1 + C \ln\left(\frac{\dot{\bar{\epsilon}}_{pl}}{\dot{\bar{\epsilon}}_0}\right) \right] \left[ 1 - \left(\frac{T - T_r}{T_m - T_r}\right)^m \right], \quad (22)$$

where  $A$ ,  $B$ ,  $C$ ,  $n$ ,  $m$  are material constants,  $\bar{\epsilon}_{pl}$ ,  $\dot{\bar{\epsilon}}_{pl}$  and  $\dot{\bar{\epsilon}}_0$  are the equivalent plastic strain, equivalent plastic strain rate and reference strain rate respectively.  $T$  is the temperature,  $T_r$  is the reference temperature and  $T_m$  is the melting temperature.

The associated flow rule, which assumes that plastic deformation occurs in the direction normal to the yield surface in the stress space is used for determining the relationship between the stress states and the plastic strain increment  $d\underline{\epsilon}^{pl}$ :

$$d\underline{\epsilon}^{pl} = d\lambda_{pl} \frac{\partial F}{\partial \underline{\sigma}}, \quad (23)$$

where  $d\lambda_{pl}$  is a non-negative scalar known as the plastic multiplier that scales with the magnitude of plastic deformation. With the von Mises yield criterion of Eq. (21) and the Johnson–Cook hardening law of Eq. (22) implemented in Eq. (23):

$$d\underline{\epsilon}^{pl} = d\lambda_{pl} \sqrt{\frac{3}{2}} \frac{\underline{S}}{\|\underline{S}\|} = d\lambda_{pl} \frac{3}{2} \frac{\underline{S}}{\sigma_y^{JC}(\bar{\epsilon}_{pl}, \dot{\bar{\epsilon}}_{pl}, T)}. \quad (24)$$

As the flow stress represented in the Johnson–Cook hardening law is not constant, this equation cannot be solved directly. Instead, with the radial return method proposed by Wilkins [68], for example, the plastic multiplier  $d\lambda_{pl}$  can be found, and the plastic strain increment as well as the deviatoric stress can be calculated. The details of how to solve this equation however is not the focus of the current study. The implementation of the radial return algorithm is elaborated in the dissertation of R othlin [66].

To effectively correlate changes in physical properties with mechanical states, an additional equation of state is needed. A simple example particularly relevant for scenarios like metal cutting where density



**Table 1**  
Mechanical and thermal properties of workpiece and tool materials in simulation [63].

| Property                            | Ti6Al4V | WC/Co  |
|-------------------------------------|---------|--------|
| Density $\rho$ [kg/m <sup>3</sup> ] | 4430    | 15 250 |
| Young's modulus $E$ [GPa]           | 110     | –      |
| Poisson ratio $\nu$ [–]             | 0.35    | –      |
| Specific heat $c_p$ [J/(kg K)]      | 526     | 292    |
| Thermal conductivity $k$ [W/(m K)]  | 6.8     | 88     |

**Table 2**  
Johnson–Cook parameters of the workpiece Ti6Al4V provided by Klippel et al. [47].

| $A$ [MPa] | $B$ [MPa] | $C$     | $m$    | $n$   | $T_r$ [K] | $T_m$ [K] |
|-----------|-----------|---------|--------|-------|-----------|-----------|
| 852.1     | 338.9     | 0.02754 | 0.5961 | 0.148 | 300       | 1836      |

changes are minimal can be represented as

$$p = \frac{K}{\rho}(\rho - \rho_0), \quad (25)$$

in which  $p$  is the hydrostatic pressure,  $K$  represents the bulk modulus. This equation introduces a method for obtaining the hydrostatic pressure, a factor previously overlooked but essential for calculating the Cauchy stress tensor in describing the stress states of materials.

The mechanical and thermal properties of the workpiece and tool are listed in Table 1. For simplicity, this study assumes that the material properties are independent of temperature. This is primarily because the variations in these property values, due to temperature changes at the tool-chip interface, are considered insignificant. Consequently, the time-consuming task of variable interpolation can be avoided, leading to enhanced computational efficiency. Moreover, simulations with constant material properties can also simplify the analysis for sensitivity analysis. The values of the JC model for the same batch of Ti6Al4V material used in this study are inversely calibrated by Klippel [47] through orthogonal cutting simulations and listed in Table 2. It is important to mention that during the inverse calibration process, a constant Coulomb friction model with a COF of 0.35 was employed.

### 2.1.3. Physical parameters at the contact

The involved domains and the heat activities at the interface are represented in Fig. 1(b). The interface between workpiece and tool is treated as a sliding contact with the exchange of mechanical and thermal energy. The frictional stress  $\tau_{fri}$  on the contact is given by the classic Coulomb or Coulomb-Amonton law in this study:

$$|\tau_{fri}| = \mu |\sigma_{cont}|, \quad (26)$$

where  $\mu$  is the coefficient of friction and  $\sigma_{cont}$  is the normal contact stress between the workpiece and cutting tool determined by the penalty method [69]. The value of  $\mu$  might be various depending on the implemented friction model. In fact, the calculation of  $\sigma_{cont}$  and  $\tau_{fri}$  is rather numerical oriented, and the details will be further discussed in Section 2.3. To distribute the frictional energy  $\dot{q}_{fri}$  into the cutting tool and workpiece separately, a contact parameter  $\beta_{fri}$  – the frictional heat partition coefficient for the cutting tool is introduced [70,71]. For the sake of distinguishing from the global heat partition effect in machining theory, “ $fri$ ” is added in the notation. Thus, the amounts of frictional heat partitioned to the tool and workpiece are given respectively as

$$\begin{cases} \dot{q}_{fri \rightarrow tool} = \beta_{fri} \dot{q}_{fri}, \\ \dot{q}_{fri \rightarrow wp} = (1 - \beta_{fri}) \dot{q}_{fri}. \end{cases} \quad (27)$$

With the given heat flow  $\dot{q}_{wp \rightarrow tool}$ , the thermal conductance resistance  $R_t$  of the tool-workpiece and tool-chip contacts is expressed as a function of the existing temperature difference between two contact surfaces:

$$R_t = \frac{\dot{q}_{wp \rightarrow tool}}{T_{wp} - T_{tool}}. \quad (28)$$

**Table 3**  
Contact parameters at tool-workpiece/chip interface in simulation [63].

| Contact parameter   | Symbol        | Value             |
|---|---------------|-------------------|
| Heat conduction coefficient on interface [W/(m <sup>2</sup> K)] | $h_c$         | 5·10 <sup>6</sup> |
| Frictional heat partition coefficient to tool [–]               | $\beta_{fri}$ | 0.5               |
| Frictional energy converted to heat [–]                         | $\eta$        | 1.0               |

The associated conductivity on the interface is thus treated as the reciprocal of aforementioned thermal impedance [70]. Typically, a parameter called heat conduction coefficient on interface  $h_c$  is used in the literature, and the local heat flow on the interface is calculated through

$$\dot{q}_{wp \rightarrow tool} = h_c (T_{wp} - T_{tool}). \quad (29)$$

It should be noted that the modeling of  $\beta_{fri}$  and  $h_c$  can be complicated. Similar to the COF, thermal contact parameters usually depend on local conditions such as material hardening state, sliding velocities, surface roughness, temperature, contact pressure, material thermal properties and so on [70,72]. For example, sliding velocity dependent phenomenological models for  $\beta_{fri}$  and  $h_c$  have been proposed and identified by various researchers in literature [9,72]. In this work, the  $\beta_{fri}$  and  $h_c$  parameters will be assumed as constants for simplification. The setups of these contact parameters can be found in Table 3.

### 2.1.4. Summary

The governing equations in strong formulations and corresponding initial and boundary conditions are summarized. For the mechanical problem:

$$\begin{cases} \frac{Dp}{Dt} = -\rho \nabla \cdot \underline{v} & \text{in } \Omega_{wp} \times ]0, t[, \\ \frac{D\underline{v}}{Dt} = \frac{1}{\rho} \nabla \cdot \underline{\underline{\sigma}} + \underline{b} & \text{in } \Omega_{wp} \times ]0, t[, \\ \frac{\partial \underline{x}}{\partial t} = \underline{v} & \text{in } \Omega_{wp} \times ]0, t[. \end{cases} \quad (30)$$

Here, the essential kinematic connection between position and velocity is added, as this equation will be further emphasized during the subsequent numerical discretization process. For the thermal problem:

$$\begin{cases} \rho c_p \frac{\partial T}{\partial t} = \text{div}(k \nabla T) + \dot{q} & \text{in } \Omega \times ]0, t[, \\ T = T_0 & \text{in } \Omega \times \{0\}, \\ T = T_0 & \text{on } \partial \Omega_{fixed} \times ]0, t[, \\ \dot{q} = \dot{q}_{plast} & \text{in } \Omega_{wp} \times ]0, t[, \\ h_c \nabla T \cdot \underline{n} = \dot{q}_{wp \rightarrow tool} & \text{on } \partial \Omega_{wp \rightarrow tool} \times ]0, t[, \\ \dot{q} = \dot{q}_{fri} & \text{on } \partial \Omega_{wp \rightarrow tool} \times ]0, t[, \end{cases} \quad (31)$$

in which  $\underline{n}$  is the normal vector on the tool-workpiece interface, and  $T_0$  is the initial temperature.

### 2.2. Numerical formulations in SPH domain

The presented formulation here only provides essential results for modeling purposes. In-depth mathematical and physical discussions of the SPH method, along with the associated continuity theory of SPH derivatives, can be found in the works of Price [73] and Monaghan [74]. Furthermore, the numerical discretization in the FEM domain for the transient thermal analysis will not be further elaborated. Details can be referred to the previous work [63].

In the SPH method, the material is discretized into particles that do not have strong spatial connections to their neighbors. The calculation of the physical domains depends only on the local particle clouds. A brief description of the SPH approximation theory is given in this section. The SPH method is based on the integral interpolant of functions:

$$f(\underline{x}) = \int_{\Omega} f(\underline{x}') W(\underline{x}' - \underline{x}, h_s) d\underline{x}', \quad (32)$$

in which  $W(\underline{x}' - \underline{x}, h_s)$  is the smoothing kernel, and  $h_s$  is the smoothing length that controls the supporting domain of each particle. A popular choice for the smoothing kernel is the cubic spline kernel:

$$W_c(\underline{x}' - \underline{x}, h_s) = \frac{n_c}{h_s^n} \begin{cases} 1 - \frac{3}{2}q^2 + \frac{3}{4}q^3 & 0 \leq q < 1, \\ \frac{1}{4}(2-q)^3 & 1 \leq q \leq 2, \\ 0 & \text{otherwise.} \end{cases} \quad (33)$$

With  $q = |\underline{x}' - \underline{x}|/h_s$ ,  $n$  is the spatial dimension and  $n_c$  is a dimension dependent constant given  $10/(7\pi)$  for two-dimensional problems. In the current study, the smooth length  $h_s$  is set as 1.5 times of the initial particle spacing. With a given spatially discretized domain, the integral form in Eq. (32) is replaced by summing up the contributions of each discrete neighboring particle  $j$ , and thus the function value at particle  $i$  is approximated:

$$\langle f(\underline{x}_i) \rangle = \sum_j f(\underline{x}_j) W(\underline{x}_i - \underline{x}_j, h_s) \Delta \underline{x}_j, \quad (34)$$

in which  $\langle \cdot \rangle$  denotes an approximated quantity in the SPH method. For simplicity, the term  $W(\underline{x}_i - \underline{x}_j, h_s)$  will be shortened to  $W_{ij}$  in this paper.

For the first derivative of a scalar variable, the direct approximating approach is given by simply deriving both sides of Eq. (34):

$$\langle \nabla f(\underline{x}_i) \rangle = \sum_j f(\underline{x}_j) \nabla W_{ij} \Delta \underline{x}_j. \quad (35)$$

Nevertheless, this direct approach leads to poor estimation of the derivatives. Two other formulations are generally preferred in terms of the conservation property in many research work [74]:

$$\langle \nabla f(\underline{x}_i) \rangle = \sum_j \frac{\phi_j}{\phi_i} [f(\underline{x}_j) - f(\underline{x}_i)] \nabla W_{ij} \Delta \underline{x}_j, \quad (36a)$$

$$\langle \nabla f(\underline{x}_i) \rangle = \sum_j \left[ \frac{\phi_j}{\phi_i} f(\underline{x}_i) + \frac{\phi_i}{\phi_j} f(\underline{x}_j) \right] \nabla W_{ij} \Delta \underline{x}_j, \quad (36b)$$

where  $\phi$  is any arbitrary differentiable scalar field variable attributed to the particle. In fact, the properties of these first derivative formulations should be highlighted. Cummins and Rudman [75] and Price [73] both hold opinions that these two forms of the first derivative actually compose a conjugate pair, and choosing one naturally tends to lead to the use of the other.

For the Laplacian operator in Eq. (31), a widely accepted discretization is given by Brookshaw [76]:

$$\langle \nabla^2 f(\underline{x}_i) \rangle = 2 \sum_j [f(\underline{x}_i) - f(\underline{x}_j)] \frac{\underline{e}_{ij}}{|\underline{x}_i - \underline{x}_j|} \cdot \nabla W_{ij} \Delta \underline{x}_j, \quad (37)$$

where a unit vector  $\underline{e}_{ij}$  between two particles is introduced in the approximation. The benefit of employing this method is that it eliminates the need for a higher order derivative of the kernel function in Eq. (37). Alternative discretization techniques for the Laplacian operator such as the Particle Strength Exchange method that can be detailed in Eldredge et al. [77] are also available. However, it is worth noting that these methods demand higher computational cost, which will not be considered in this study.

As a result, the discretized governing equations for the workpiece domain are presented:

$$\begin{cases} \langle \dot{\rho}_i \rangle = -\rho_i \sum_j (\underline{v}_j - \underline{v}_i) \cdot \nabla W_{ij} \frac{m_j}{\rho_j}, \\ \langle \dot{\underline{v}}_i \rangle = \sum_j \left( \frac{\underline{\sigma}_i}{\rho_i^2} + \frac{\underline{\sigma}_j}{\rho_j^2} \right) \cdot \nabla W_{ij} m_j + \frac{b_i}{m_i}, \\ \langle \dot{\underline{x}}_i \rangle = \underline{v}_i, \\ \langle \dot{T}_i \rangle = 2 \frac{k}{\rho_i c_p} \sum_j (T_i - T_j) \frac{\underline{e}_{ij}}{|\underline{x}_i - \underline{x}_j|} \cdot \nabla W_{ij} \frac{m_j}{\rho_j} + \frac{\dot{q}}{\rho_i c_p}. \end{cases} \quad (38)$$

Here,  $\rho$  is the scalar variable selected in the first derivative estimation in Eq. (36). The estimation of the continuity equation adopts the first form, whereas the momentum conservation equation is discretized

using the second form. Importantly, these derivations can also be obtained through the Hamiltonian system, which inherently ensures the preservation of conservation laws. Thus, the selection of the first derivative estimation in governing equations is not arbitrary but contains fundamental physical principles. Details can be referred to Price [73]. However, the author reveals a paradoxical observation: preserving the momentum conservation property in its mathematical formulation results in larger linear errors compared to employing direct derivatives, as indicated in Eq. (35), despite the latter's lack of momentum conservation. This counterintuitive outcome may be attributed to the principle of least action inherent to Hamiltonian systems. This principle suggests that particles possess an "intrinsic" tendency towards more optimal arrangements, thereby minimizing system errors. In contrast, the approach using direct derivatives exhibits greater sensitivity to particle distribution, potentially leading to even larger inaccuracies at the end. Stabilizers such as the artificial viscosity (a.v.) [78], the artificial stress (a.s.) [79] and the XSPH correction [80] are implemented in the mechanical domain in order to mitigate the tensile instability, which is characterized by the occurrence of particle clustering and dispersal [81]. The brief formulations and the setup of the related parameters are provided in Appendix.

The leapfrog integration is employed for both the SPH and FEM domains in the cutting simulation, consistent with prior SPH simulation work in the iwfmfree. The implementation details can be referred to the original work by R othlin [62]. Note that this study does not incorporate crack modeling as described in [82], given that shearing is the primary mechanism in the chip formation process for ductile machining.

### 2.3. Numerical contact modeling in SPH-FEM cutting simulation

To understand the behavior of friction models in simulations, it is important to revisit the contact modeling approach. In this study, the normal contact force is modeled using a penalty method, which was originally proposed by Nianfei et al. [83]:

$$\underline{f}_{-p}^{cont} = \kappa \frac{m_p \cdot g_N}{\Delta t^2} \underline{n}, \quad (39)$$

in which  $\kappa$  is a numerical parameter named as interface stiffness constant and set to 0.01,  $m_p$  is the particle mass,  $g_N$  is the penetration depth of the particle,  $\Delta t$  is the time increment and  $\underline{n}$  is the normal vector of the surface. The illustration of calculating the normal contact force is referred to Fig. 2. Once the normal contact force has been determined, the friction force acting on each particle can be calculated using a straightforward approach:

$$|\underline{f}_{-p}^{fri}| = \mu |\underline{f}_{-p}^{cont}|. \quad (40)$$

The calculated frictional force will be given the negative direction of the relative sliding speed. However, this implementation might lead to a highly oscillatory behavior in particles, particularly when the calculated frictional stress becomes unrealistically large so that a change in the sliding direction is induced. To overcome this instability issue, specific measures need to be implemented. One approach suggested in the LS-DYNA manual [84] involves calculating a trial force vector prior to applying the frictional force:

$$\underline{f}_{-p}^* = \underline{f}_{-p}^{fri,old} - \underline{v}_{-p}^{rel} \cdot m_p / \Delta t, \quad (41)$$

where  $\underline{f}_{-p}^{fri,old}$  is the frictional force vector computed from the previous time increment. This trial force vector is an estimation of the force required to bring the particle's relative sliding to a halt at the contact. The local frictional force is then determined by comparing the trial force calculated in Eq. (41) to the nominal value calculated in Eq. (40):

$$\underline{f}_{-p}^{fri} = \begin{cases} \mu |\underline{f}_{-p}^{cont}| \cdot \underline{f}_{-p}^* / |\underline{f}_{-p}^*| & \text{if } |\underline{f}_{-p}^*| > \mu |\underline{f}_{-p}^{cont}|, \\ \underline{f}_{-p}^* & \text{if } |\underline{f}_{-p}^*| \leq \mu |\underline{f}_{-p}^{cont}|. \end{cases} \quad (42)$$

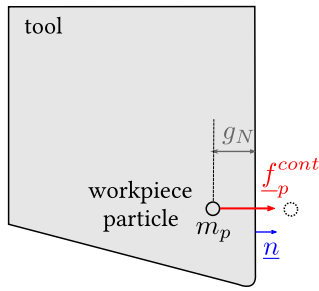


Fig. 2. Illustration of the penalty contact method. When the SPH particle is detected inside the tool domain, the penetration depth  $g_N$  is calculated, and a “repulsive” contact force is calculated with the consideration of the surface normal vector  $\underline{n}$ .

Table 4

Tested physical parameter dependent friction models, units of  $T$ ,  $v_{rel}$  and  $\sigma_n$  are K, m/s and GPa respectively.

| No. | Model  | Notes                                |
|-----|--|--------------------------------------|
| 1   | $\mu(T) = 0.51 \cdot [1 - (\frac{T - T_r}{T_p - T_r})^{5.76}]$   | Calibration from [85]                |
| 2   | $\mu(T) = 0.51 \cdot [1 - (\frac{T_p - T}{T_p - T_r})^{0.5961}]$ | Thermal softening term from JC model |
| 3   | $\mu(T) = 0.51 \cdot [1 - (\frac{T_m - T_r}{T_m - T_r})^2]$      | Dummy model                          |
| 4   | $\mu(T) = 0.3 \cdot [1 + (\frac{T_m - T_r}{T_m - T_r})^2]$       | Inverse trend of Model 3             |
| 5   | $\mu = 0.334 \cdot  v_{rel} ^{-0.154}$                           | Calibration from [85]                |
| 6   | $\mu = 0.334 \cdot  v_{rel} ^{0.154}$                            | Inverse trend of Model 5             |
| 7   | $\mu = 0.2 \cdot \sigma_n^{-0.5}$                                | Dummy model                          |
| 8   | $\mu = 0.25 \cdot \sigma_n^{0.5}$                                | Inverse trend of Model 7             |

The above-presented friction modeling only considers the natural constraints such that the friction cannot change the sliding direction of the target on the interface and operates on the force level of each particle. With the obtained forces in Eqs. (39) and (42), the normal contact stress  $\sigma_n$  and the frictional stress  $\tau_f$  can be calculated through

$$\begin{cases} \sigma_n = \frac{f_p^{cont}}{\Delta x_i}, \\ \tau_f = \frac{f_f^{cont}}{\Delta x}, \end{cases} \quad (43)$$

in which  $\Delta x$  represents the distance between particles. To simplify the notation, the vector notation is dropped, and the magnitudes  $\sigma_n$  and  $\tau_f$  are used in the subsequent discussions. When the frictional stress is additionally limited by the shear flow stress, a comparison similar to Eq. (3) is introduced as

$$\tau_f = \min(\bar{\tau}_p, \frac{|f_f^{cont}|}{\Delta x}). \quad (44)$$

in which  $\bar{\tau}_p$  is the local shear flow stress of the particle.

#### 2.4. Friction models implemented in cutting simulations

To study the influence of friction modeling on the simulated chip formation process, a sensitivity analysis is conducted using a constant COF value based on the Coulomb friction model. The COF value is varied from 0 to 1 to examine the effect of friction on the simulated chip formation process. The effects of the shear flow stress limit are also examined.

Subsequently, friction models that consider physical parameters such as the relative sliding velocity  $v_{rel}$ , temperature  $T$ , and normal stress  $\sigma_n$  are implemented. The impact of these models on the results of the cutting simulations is then examined to assess their effects and effectiveness in metal cutting simulations. Table 4 provides a detailed list of these dummy friction models. To elaborate further, Model 1 and Model 5 are taken from the experiment-simulation calibration work

by Afrasiabi et al. [85] and presented respectively in the forms of Eqs. (4) and (8). Model 2 represents the softening term of the Johnson–Cook model presented in Table 2. The remaining models and their constants have been artificially adjusted irrespective of the physical interpretations. Models 3 and 4 demonstrate opposite trends in their response to temperature variations within the range of 1000 to 1200 K. Model 6 incorporates the relative sliding velocity  $v_{rel}$  as a parameter and exhibits a distinct trend that differs from Model 5. To account for the absence of a pressure-dependent friction model for Ti6Al4V machining, two exponential functions with contrasting trends referred to as Model 7 and Model 8 have been proposed. These models utilize the term in Eq. (5) to incorporate the pressure dependence of the frictional behavior. Fig. 3 provides graphical representations of these models to better highlight their dependencies on physical parameters. Furthermore, an upper limit of 0.8 has been imposed on Models 5 and 7 to prevent excessively large COF values.

### 3. Auxiliary cutting experiments

Quasi-orthogonal cutting tests are performed in this study. The Ti6Al4V workpiece is prepared as a hollow cylinder with a thickness of 2 mm and is clamped on the spindle of a Schaublin 42L CNC lathe. The hardness of the workpiece is approximately 310 HV10. Uncoated turning inserts CCMW 09 T3 04 H13 A from Sandvik Coromant are used as cutting tools in the experiment. No coolant or lubricant is used during the tests. The graphical illustration of the experimental setup can be referred to Fig. 4. The cutting force  $F_c$  and feed force  $F_f$  are measured using a Kistler dynamometer type 9121A5 in combination with a Kistler 5019 A charge amplifier and a NI USB-6211 data acquisition system, and later normalized to specific values with units of N/mm. To mitigate the influence of tool wear on the process forces, the force analysis considers only the dynamometer signals recorded during the second or up to the third rotation of the workpiece. The detailed information on workpiece preparation and the cutting insert, as well as the signal processing is available in Klippel et al. [86]. The process parameters for the cutting experiment are summarized in Table 5, and the force results are summarized in Table 6. Specifically, segmented chips are obtained in all tests except under the condition when  $h = 0.01$  mm. The authors acknowledge that the chosen cutting parameters, particularly the high cutting speed, exceed current industrial used ones for titanium machining. The rationale for choosing these parameters is to facilitate rapid computations, thereby enabling a more generalized understanding of the effects of friction modeling in metal cutting simulations.

Examples of the insert after the cutting test are depicted in Fig. 5, and the high-speed camera videos of the cutting tests can be viewed in the provided link [86]. A significant area of Ti alloy is observed to adhere to the insert’s rake face under a Sensofar® S neox 5 axis optical microscope. It is improbable that this Ti material was spattered onto the insert from the contact side of the chip during the cutting experiment, as the surface of the rake face shows distinct signs of abrasion. After etching the inserts with oxalic acid, the rake faces are inspected using a Hitachi® SU5000 scanning electron microscope (SEM), revealing a narrower contact band or wear marks when compared to the Ti-covered area before etching, as shown in Fig. 5. According to the video recording, it is likely that the wavering motion of the long continuous chip contributes to the elongation of the contact length. The distinction between these two contact areas will be further discussed in the subsequent sections.

Fig. 6 presents a illustration of an experimental result of a segmented chip generated at a cutting speed of 318 m/min and an uncut chip thickness of 0.1 mm, against an exemplary simulation result employing a constant Coulomb friction model with a COF of 0.35. Shear flow stress limit is not applied in the friction modeling. The comparative analysis reveals average maximum chip thicknesses of 134.92  $\mu\text{m}$  for the experimental setup and 145.77  $\mu\text{m}$  for the simulation, alongside average minimum thicknesses of 72.23  $\mu\text{m}$  and 89.92  $\mu\text{m}$ , respectively.

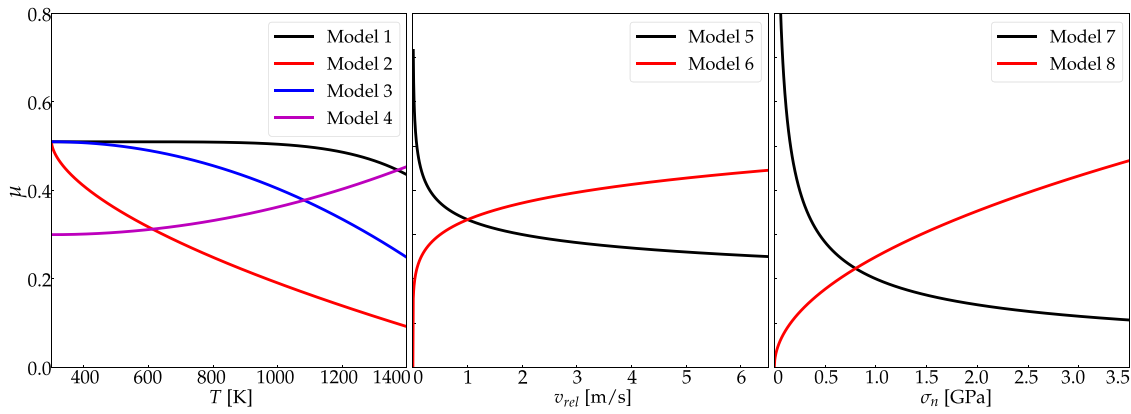


Fig. 3. Graphical representation of tested friction models in Table 4 that are dependent on  $T$ ,  $v_{rel}$  and  $\sigma_n$ . Note that in Model 5 and 7, the  $\mu$  values tend to approach infinity. Therefore, an upper limit of 0.8 is applied in the simulation.

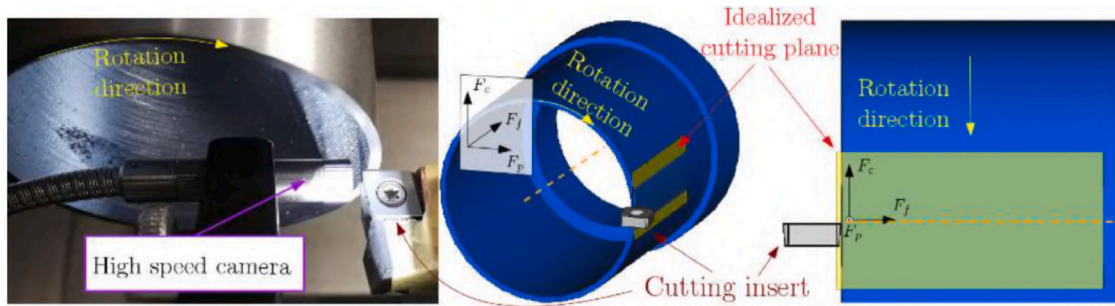


Fig. 4. Setup of the quasi-orthogonal cutting test [86]. The reference plane intersects the central axis of the cylindrical workpiece, allowing the turning process to be approximated as the orthogonal cutting. In addition to the cutting force  $F_c$  and the feed force  $F_f$ , the force component  $F_p$  oriented along the radial direction of the workpiece is generally considered negligible in this quasi-orthogonal cutting test.

Table 5  
Process parameters of Ti6Al4V orthogonal cutting experiments.

| Rake angle $\gamma$ [°]     | Clearance angle $\alpha$ [°]  | Cutting edge radius $r_n$ [ $\mu\text{m}$ ] |
|-----------------------------|-------------------------------|---|
| 0                           | 7                             | 35  |
| Cutting speed $v_c$ [m/min] | Uncut chip thickness $h$ [mm] |   |
| 190, 254, 318               | 0.01, 0.1, 0.2, 0.4           |   |

Table 6  
Experimental results of specific cutting forces reprocessed according to [86].

| $v_c$ [m/min] | $h$ [mm] | $F_c$ [N/mm] | $F_f$ [N/mm] |
|---------------|----------|--------------|--------------|
| 190           | 0.01     | 40.00        | 78.24        |
| 190           | 0.1      | 162.87       | 115.56       |
| 190           | 0.2      | 272.57       | 150.33       |
| 190           | 0.4      | 465.14       | 214.72       |
| 254           | 0.01     | 38.73        | 72.77        |
| 254           | 0.1      | 155.87       | 114.90       |
| 254           | 0.2      | 264.16       | 139.00       |
| 254           | 0.4      | 439.08       | 199.26       |
| 318           | 0.01     | 34.68        | 67.86        |
| 318           | 0.1      | 149.46       | 99.22        |
| 318           | 0.2      | 256.06       | 143.14       |
| 318           | 0.4      | 436.51       | 216.88       |

While the simulation decently mirrors the chip geometries, it is necessary to clarify that the direct comparison of simulated and experimental results is not the major focus of this research. Instead, the study aims to examine the effects and behaviors of established friction models and does not endeavor to conduct an in-depth validation of simulation results against experimental data.

## 4. Simulation results

This section firstly presents a sensitivity analysis based on varying the COF when employing a constant Coulomb friction model in simulations. The effects of limiting the frictional stress by shear flow stress are also examined. Additionally, friction models that depend on physical parameters are applied, with their simulation outcomes compared. Finally, the discussion revisits topics from the literature review, including the impact of friction modeling on contact conditions, the application of the shear flow stress friction model and possible causes for inaccurately predicted feed forces.

### 4.1. Cutting simulations with constant Coulomb friction model

The sensitivity study is conducted under the conditions of  $v_c = 318$  m/min and  $h = 0.2$  mm with the aim of achieving a quick computation. The simulated cutting distance is up to 0.6 mm, a length sufficient to generate multiple chip segments and modify temperature distribution on the tool surface acquired from the previous long-distance chip formation simulation to the new stable state. Given different  $\mu$  values, Fig. 7 shows the simulated physical contact variables including  $\sigma_n$ ,  $\tau_f$ ,  $v_{rel}$ ,  $T$ , the power density term  $\tau_f v_{rel}$  and the effective COF value  $\mu_{eff}$  calculated by  $\tau_f / \sigma_n$ . As the overall contact area varies dynamically

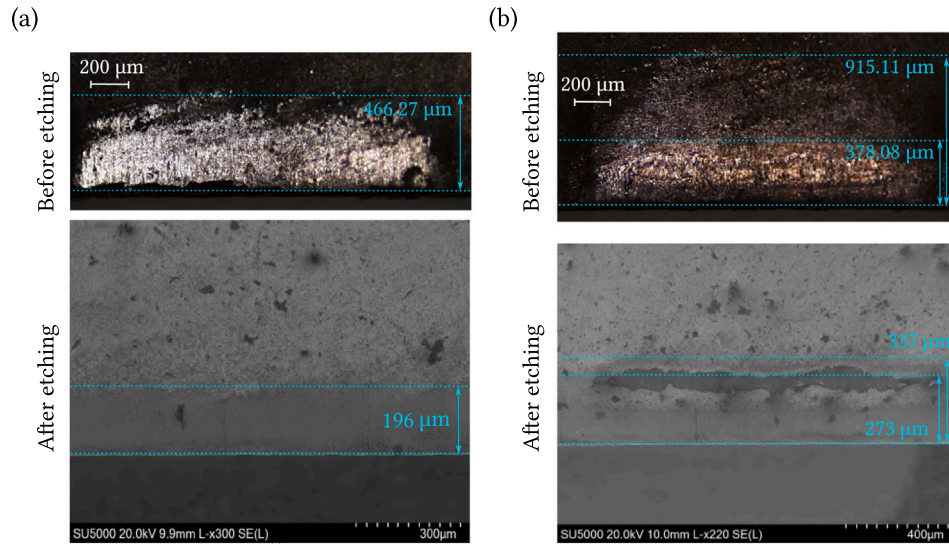


**Fig. 5.** Images of the insert's rake faces after cutting experiments under two different cutting conditions: (a)  $v_c = 318$  m/min,  $h = 0.1$  mm, and (b)  $v_c = 318$  m/min,  $h = 0.2$  mm. The high speed video recordings corresponding to each set of process parameters available for reference through hyperlinks [video1](#) and [video2](#). Prior to etching, the bright color on the insert's surface indicates the presence of an adhered layer. After the etching process, the "major" contact area becomes discernible due to the color contrast or visible crater wear mark in SEM images.

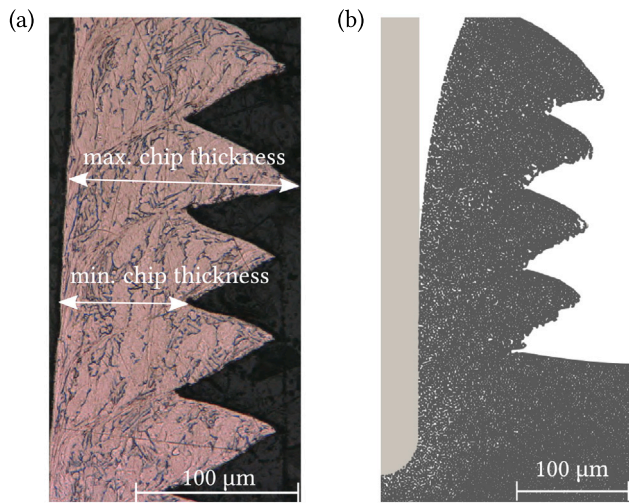


**Fig. 6.** Exemplary images of the segmented Ti6Al4V chip from (a) cutting test and (b) exemplary simulation results. The cutting speed is 318 m/min and the uncut chip thickness is 0.1 mm. Note that a constant Coulomb friction model with the COF as 0.35 is used in the exemplary simulation, and the frictional stress is not limited by local shear flow stress.

during the segmented chip formation, these contact variables are averaged during the chip formation process and shown locally on the tool surface. Fig. 8 exhibits the simulated average contact length  $l_c$  on the rake face given different  $\mu$  values. Fig. 9 and Fig. 11 depict the distribution of equivalent plastic strain  $\bar{\epsilon}_p$  and the velocity field of the workpiece material in the  $y$  direction (perpendicular to the machined surface) at four different stages of chip segment formation, without and with the shear flow stress limit, respectively. To provide a clearer explanation, it is necessary to define several contact states in advance. The interface between the tool and the chip or work material can be physically divided into elastic and plastic regions according to the material states of the chip's contact side. In the elastic contact region, there is no velocity gradient in the direction perpendicular to the chip's contact surface, and the material is not hardened due to friction. On the contrary, for the plastic contact, there exists local plastic deformation

on the chip's contact surface. From a kinematic perspective, the contact region can be further divided into two distinct parts: the sliding part and the sticking part. In the sliding part, the chip material is capable of moving relative to the tool. In the sticking region, the relative motion between the chip and the tool surface is minimal, leading to a scenario where the chip material appears to adhere to the tool and shears internally. It is important to note that whenever the  $v_{rel}$  value is near zero, the local chip material is considered to be adhering to the tool surface. In reality,  $v_{rel} = 0$ , i.e. the constant adhesion of material to the tool occurs only when a stable build-up edge is established. Especially, there is a specific area known as the permanent sticking zone where the magnitude of the relative sliding speed between the chip and the tool remains consistently zero or close to zero throughout the chip formation process. It should be noted that in Fig. 7, there are some contact regions where the sliding velocity is nearly uniformly distributed. In such cases, it is possible that these regions can consist of elastic contact, or a combination of both elastic and plastic contacts, as illustrated in Fig. 7. Solely relying on the sliding speed profile thus is not sufficient to accurately determine the physical contact state in these regions.

#### 4.1.1. Chip formation behaviors when frictional stress is not limited by shear flow stress

When  $\mu$  is assigned a small value of 0.05, the normal contact stress  $\sigma_n$  increases gradually from the end of the tool-chip contact area to the cutting edge and reaches the maximum value of approximately 1.6 GPa at the cutting edge. Conversely, the relative sliding velocity  $v_{rel}$  exhibits an opposite trend and decreases to a minimum value at the cutting edge. In the majority of the tool-chip contact area on the rake face, the relative sliding velocity  $v_{rel}$  remains nearly constant, and the effective coefficient of friction  $\mu_{eff}$  remains constant at 0.05 throughout the contact area. This indicates that the chip slides with little resistance, and the elastic contact region occupies a large part of the contact area. The decrease in the relative sliding velocity  $v_{rel}$  does not necessarily indicate the presence of plastic contact due to the serrated chip formation. Nonetheless, the equivalent plastic strain  $\bar{\epsilon}_p$  at the contact side of the chip in Fig. 9 suggests the occurrence of plastic contact. Note that the minimum  $v_{rel}$  around the cutting edge is close to 1 m/s, which indicates that there is no sticking zone formed in this scenario. This observation is further supported by the velocity field shown in Fig. 9.

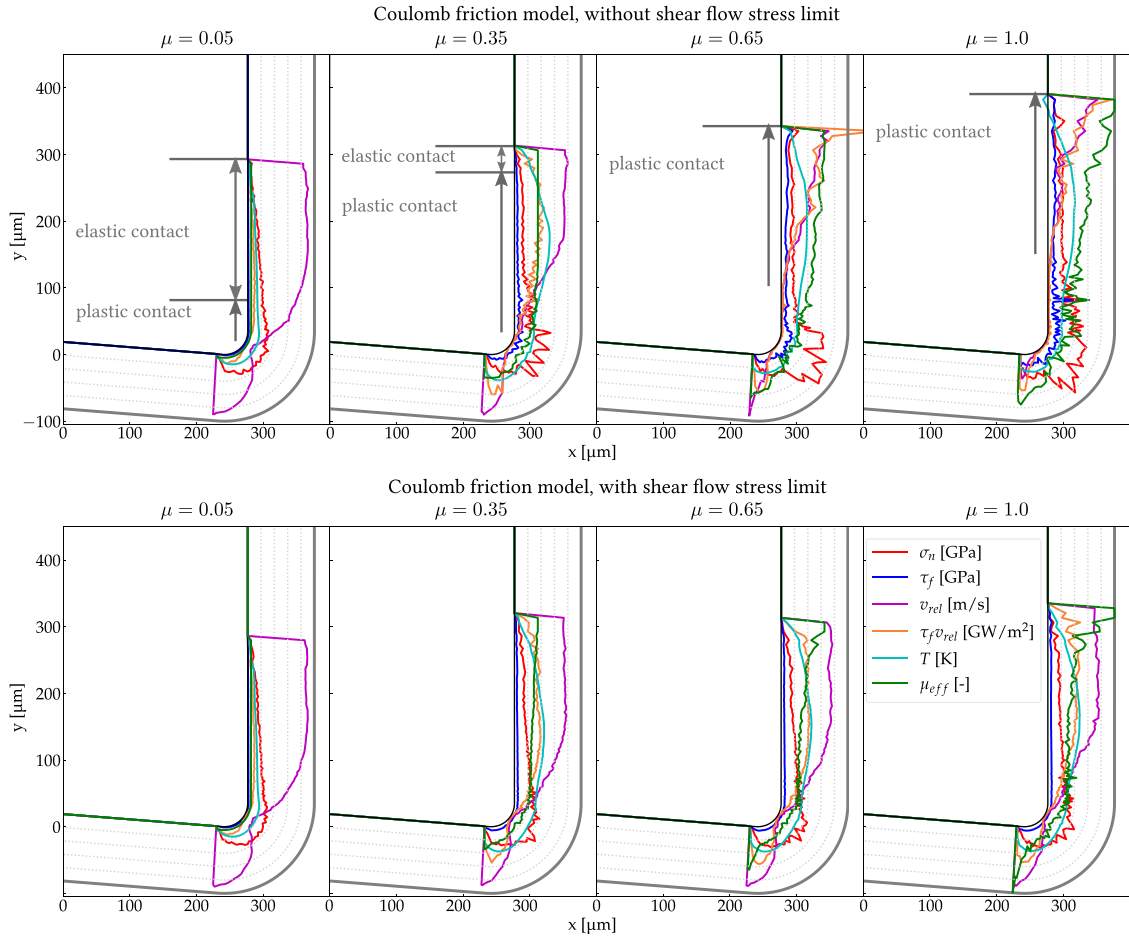


**Fig. 7.** Distribution of variables including  $\sigma_n$ ,  $\tau_f$ ,  $v_{rel}$ ,  $\tau_f v_{rel}$ ,  $T$  and  $\mu_{eff}$  at the contact region when different  $\mu$  of Coulomb friction model are implemented in the simulation.  $v_c = 318$  m/min,  $h = 0.2$  mm. While the tool surface indicates zeros for  $\sigma_n$ ,  $\tau_f$ ,  $v_{rel}$ ,  $\tau_f v_{rel}$  and  $\mu_{eff}$ , and 900 K for  $T$ . The outer solid gray line represents the maximum scale of each variable:  $\sigma_n$ ,  $\tau_f = 4$  GPa,  $v_{rel} = 6$  m/s,  $\tau_f v_{rel} = 2.0$  GW/m<sup>2</sup>,  $T = 1500$  K and  $\mu_{eff} = 1$ . The temperature curve inside the tool surface indicates values below 900 K. When the frictional stress is not limited by shear flow stress, the elastic and plastic contacts are roughly identified by comparing the  $\mu_{eff}$  values with scenarios where the shear flow stress limit is applied. For  $\mu$  exceeding 0.65, despite  $\mu_{eff}$  potentially matching the specified  $\mu$ , this scenario is typically confined to the last contacted mesh edge where normal contact stress is very small. Consequently, this specific region is classified as plastic contact along with the majority of the contact zone. Without the shear flow stress limit, the highest  $\sigma_n$  values are identified near the cutting edge, showing approximate smoothing values of 1.6, 2.4, 3.3, and 3.2 GPa for  $\mu = 0.05$ , 0.35, 0.65, and 1.0 respectively. Nevertheless, caution should be exercised when interpreting these maximum  $\sigma_n$  values, as noise due to extreme contact forces may introduce instability. Therefore, focusing on the relative trend is advised for comparisons.

As  $\mu$  is increased to 0.35, there is an increase in the contact length on the rake face. A minor decrease in the maximum value of the relative sliding velocity  $v_{rel}$  is also detected. As  $v_{rel}$  descends to zero at the cutting edge, a sticking region starts to appear. Due to the occurrence of local stagnation, the normal contact pressure  $\sigma_n$  in that particular area undergoes a significant increase and exceeds 2 GPa. The frictional stress  $\tau_f$  reaches a plateau after surpassing a certain level regardless of the magnitude of  $\sigma_n$ , even though it is not limited by the local shear flow stress. This behavior is attributed to the regulation in Eq. (42), which prevents the local material from sliding backward. As a result,  $\mu_{eff}$  deviates from the assigned value. This also indicates the presence of plastic contact regions. Fig. 9 illustrates the formation of a shear layer at the contact side of the chip, where the equivalent plastic strain  $\bar{\epsilon}_p$  reaches a magnitude comparable to that observed in the primary deformation zone. Additionally, the velocity field depicted in Fig. 9 provides evidence that the sticking region undergoes dynamic changes during the chip formation process, as well as confirms the existence of a permanent sticking region around the cutting edge.

As the value of  $\mu$  is increased to 0.65, the contact region on the rake face expands upwards, and the averaged value in Fig. 8 which is 296  $\mu\text{m}$  becomes more closely aligned with the length shown in Fig. 5 (b) from the cutting test. From the  $v_{rel}$  value in Fig. 7, a new situation appears that there is no permanent elastic contact region, and

instead, plastic contact occurs across most of the contact area. As more materials stagnate, the normal pressure continues to increase, with the obtained maximum value reaching 3.2 GPa. According to the velocity field in Fig. 9, the permanent sticking zone further enlarges on the rake face, and a thin layer of chip material appears to adhere to that area. Additionally, the thickness of the second deformation zone at the contact side of the chip increases significantly. In contrast to the results obtained with smaller  $\mu$  values, the shear plane starting from the clearance face side of the cutting edge exhibits notable upward bending during chip segmentation. This is attributed to the deformation gradient across the chip's cross-section. Furthermore, the increased friction also results in a larger chip thickness, which can be qualitatively observed in Fig. 9.

When setting  $\mu$  to 1.0, the contact length further increases. The distributions of physical variables shown in Fig. 7 and the chip flow behavior in Fig. 9 are similar to those obtained when  $\mu$  is set to 0.65. It is suggested that once the  $\mu$  value reaches a sufficiently high level, plastic contact occurs across the entire tool-chip contact region, and  $\mu_{eff}$  deviates significantly from the designated value throughout the region.

Moreover, several complementary points need to be emphasized. Firstly, the temperature field in Fig. 7 requires additional explanation. For a better comparison, Fig. 10 (a) further illustrates the simulated

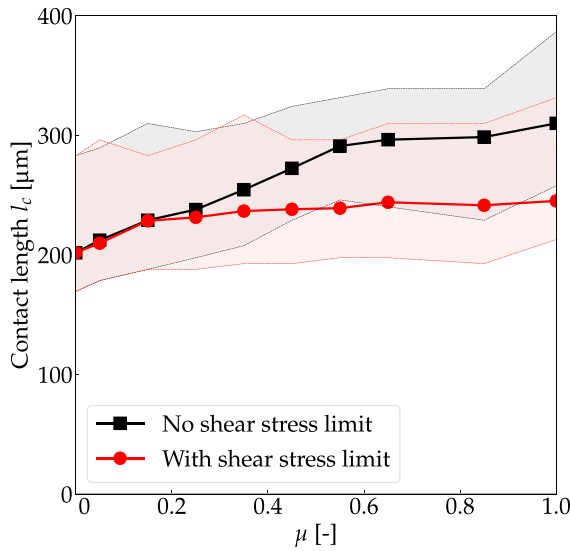


Fig. 8. The simulated average contact length  $l_c$  when different values of  $\mu$  are implemented in the Coulomb friction model. The shaded areas represent the range of  $l_c$  derived from generated simulation data in each respective case.

temperature distribution on the tool's rake face with different  $\mu$  values. When  $\mu = 0.05$ , the frictional stress is sufficiently low, resulting in the maximum temperature being concentrated around the cutting edge. As  $\mu$  increases to 0.25, the temperature rises significantly, and the hottest region shifts away from the cutting edge to the rake face. This temperature trend follows the variation in the power density term  $\tau_f v_{rel}$  in Fig. 7 as well. As  $\mu$  increases from 0.25 to 0.45, the position of the maximum temperature continues to shift along the rake face, while the temperature magnitude remains relatively consistent. However, when  $\mu$  is raised beyond 0.45, the position of the maximum temperature is no longer changed, and the temperature magnitude remains stable or even slightly decreases. The reason is that due to the increase of friction, the relative sliding term  $v_{rel}$  decreases, and thus the location of the maximum power density term  $\tau_f v_{rel}$  shifts upwards to the end of the tool-chip contact region. Consequently, the influence of heat conduction from the chip to the tool becomes more pronounced in this case, and the distribution of the tool surface temperature deviates from the pattern of  $\tau_f v_{rel}$  at the contact. Secondly, as the  $\mu$  value increases, the average contact length  $l_c$  tends to increase. However, once the applied friction reaches a certain threshold, the rate of increase in the contact length becomes smaller. When the level of friction becomes sufficiently high, plastic contact starts reaching the end of the tool-chip contact area, leading to greater resistance in chip flow. As this plastic contact approaches covering the entire contact area, any additional rise in frictional stress results in more pronounced internal shearing, particularly in the material at the end of the tool-chip contact zone, to allow the chip to “escape” from the tool surface. The difficulties in counteracting the rise in friction becomes larger, leading to a slowdown in the expansion of the contact length. It is important to note that due to the constrained simulated cutting distances, the segmented chip formation, as well as the dynamic process behavior, the maximum and minimum contact lengths obtained from simulations can vary stochastically. Therefore, the boundary values shown in Fig. 8 should only be considered as trend references. Thirdly, the impact of friction modeling on the segment generation should be further elaborated. The initiation of a new segment, which is represented in the first clip of each row in Fig. 9, demonstrates a combined effect of friction-induced sliding restriction and thermal softening of the workpiece material. This effect has been reported in [62,87]. Similar to the formation of a continuous chip, larger friction restricts the chip flow, thus accumulating more

material to form a thicker chip during the initiation stage. By qualitatively assessing the chip segments depicted in Fig. 9, it is revealed that both maximum and minimum thicknesses exhibit a very close increasing magnitude of approximately  $7 \mu\text{m}$  as  $\mu$  increases from 0.05 to 0.65. Simultaneously, a slight reduction in the shear angle is observed, leading to a decrease in the frequency of chip segmentation under conditions of increased friction. Therefore, considering the potential impacts of changing friction conditions on machining stability is also important during the cutting process.

Some artifacts such as local “ripples” exist in the SPH workpiece in Fig. 9 when the frictional stress becomes too large on the tool-chip contact, as seen in the velocity field result when  $\mu = 1$ . This can be attributed to the tensile instability issue [81] intrinsically existing in the SPH method that particles exhibit some clustering and dispersing behaviors. Although stabilizers were employed in the SPH domain as described in [62], they may not be sufficient to fully “smooth” the velocity field when the particles are subjected to extremely high external forces.

#### 4.1.2. Chip formation behaviors when frictional stress is limited by shear flow stress

When  $\mu = 0.05$ , the limitation of friction by the local shear flow stress has nearly no impact on the chip formation according to the comparison between Figs. 9 and 11. This suggests that the frictional stress over the contact has not yet reached the shear flow stress of the local material. With an increase in  $\mu$  to 0.35 and beyond, the impact of the shear flow stress limit becomes evident. This is observed through the deviation of  $\mu_{eff}$  from its prescribed value. Therefore, the subsequent analysis is only based on the results obtained when  $\mu$  is equal to or greater than 0.35.

Similar to the case when the frictional stress is not limited by the shear flow stress, increasing the friction coefficient  $\mu$  still results in a marginal rise of the simulated contact length and a decrease in the maximum value of the relative sliding velocity  $v_{rel}$ . However, there are significant differences worth emphasizing. Firstly, regardless of the assigned value of  $\mu$ , there is an evident expansion of the elastic contact region. The sticking zone around the cutting edge that is attributed to geometric constraints does not expand further with increasing  $\mu$  as shown in Fig. 11. Secondly, the distribution pattern and magnitude of the normal stress  $\sigma_n$  exhibit very little differences with changes in  $\mu$ , and the magnitude of  $\sigma_n$  at the cutting edge is considerably lower compared to the results without the shear flow stress limit. The distribution of the frictional stress  $\tau_f$  is predominantly influenced by the material local shear flow stress and demonstrates a relatively uniform pattern across the majority of the contact region. As a result, when  $\mu$  values surpassing 0.35 are applied, the temperature distribution displayed in Fig. 10 (b) exhibits strong similarity, and the  $T$  value closely aligns with the trend of  $\tau_f v_{rel}$  in Fig. 7. Most importantly, the sheared layer observed at the chip's contact side in Fig. 11 is significantly thinner when compared to cases where the friction is not limited by the shear flow stress in Fig. 9. Additionally, the magnitude of the equivalent plastic strain  $\bar{\epsilon}_p$  in this region is noticeably smaller.

Indeed, with the shear stress limit, the change in the  $\mu$  value on the simulated physical contact states in Fig. 7 is more pronounced at the end part of the contact region on the rake face. In the rest of the tool-chip contact area, the simulated physical contact states tend to remain similar, regardless of the alteration of the applied  $\mu$ , which is confirmed by the comparable magnitude of the  $\mu_{eff}$ . Therefore, the slight variations in frictional stress at the end of the tool-chip contact area lead to differences in both the thickness of the sheared layer and the extent of material hardening on the chip's contact side, as shown in Fig. 11.

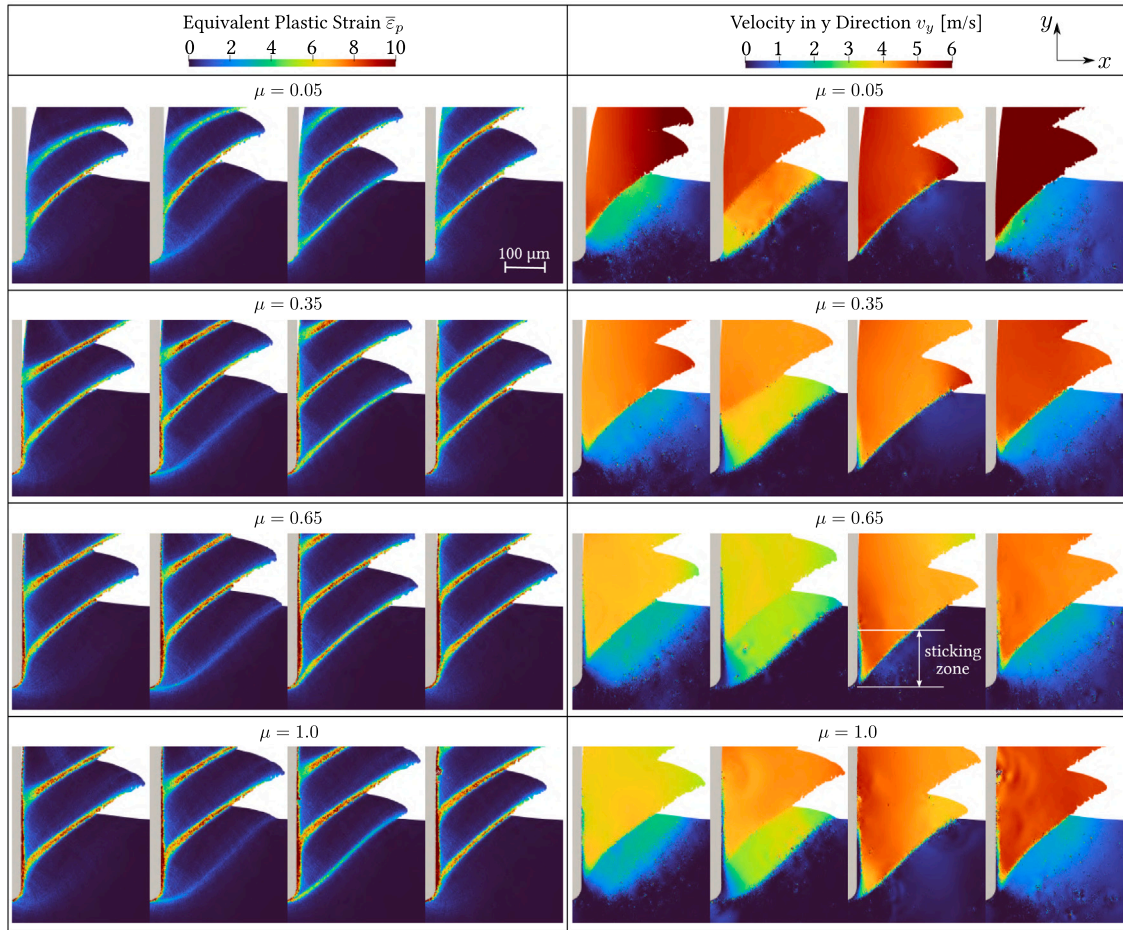


Fig. 9. Simulated equivalent plastic strain  $\bar{\epsilon}_p$  and velocity field in  $y$  direction when different  $\mu$  in the Coulomb friction model is used.  $v_c = 318$  m/min,  $h = 0.2$  mm. The frictional stress is not limited by the shear flow stress. The four clips illustrate the sequential stages of a segment formation, starting with the initiation of the shear band, followed by the material slipping along the shear band, and the upward flow of the segment. Besides, a sticking zone is indicated in the figure for illustrative purpose.

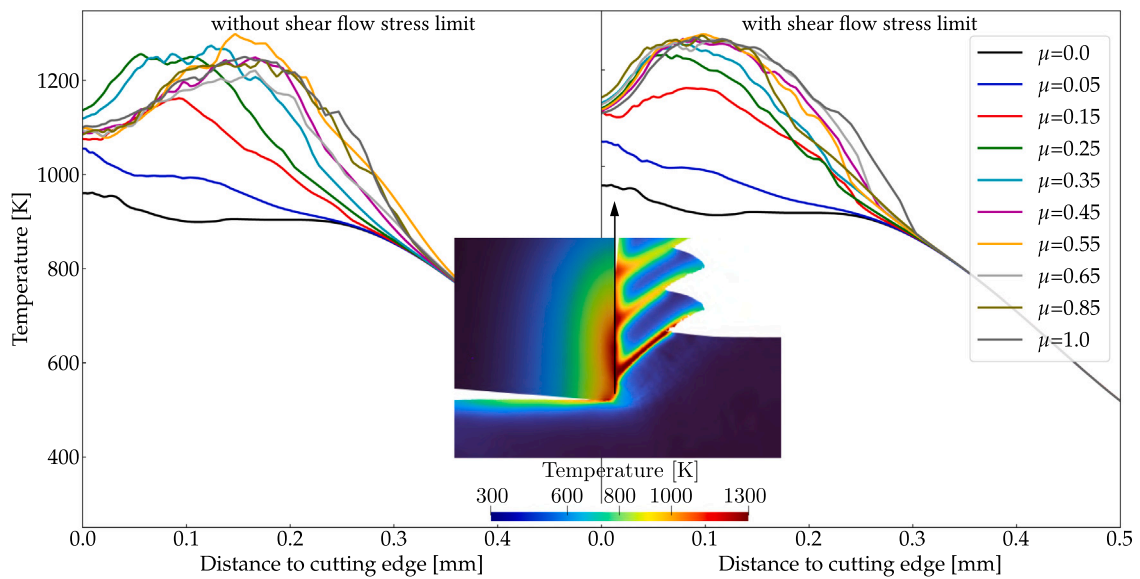


Fig. 10. The temperature profile on the tool rake face (exclude the cutting edge region) along the direction indicated by the black arrow given different  $\mu$  values in the simulation. The results are compared between the conditions when the frictional stress is not and is limited by the local shear flow stress. An illustrative thermal profile is presented with a coefficient of friction  $\mu$  of 0.35 without the shear flow stress limit.



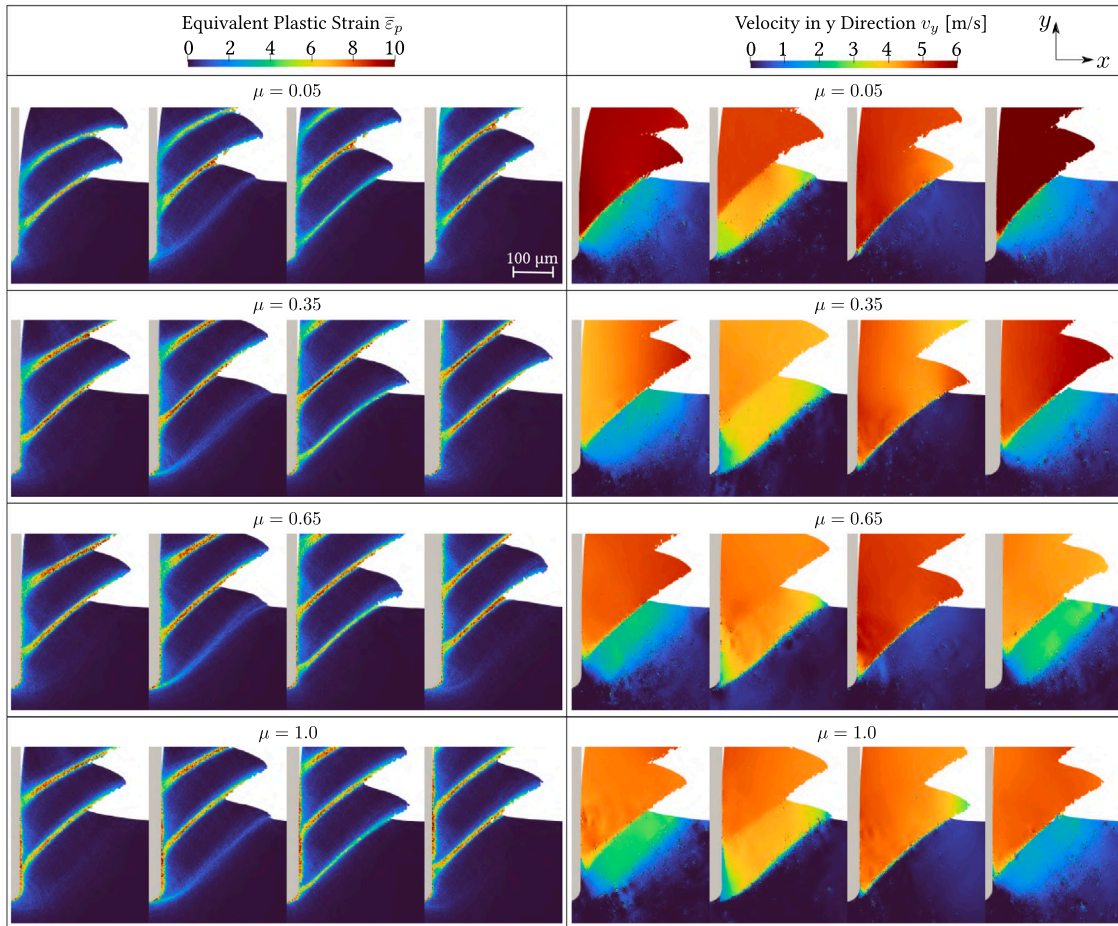


Fig. 11. Simulated equivalent plastic strain  $\bar{\epsilon}_p$  and velocity field in y direction when different  $\mu$  in the Coulomb friction model is used.  $v_c = 318$  m/min,  $h = 0.2$  mm. The frictional stress is limited by the shear flow stress. The four clips demonstrate the sequential stages of a segment formation.

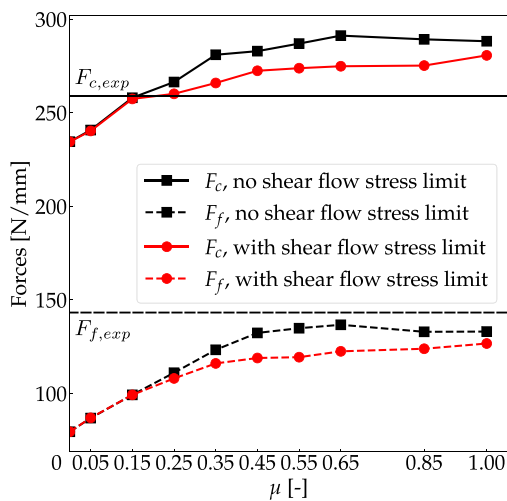


Fig. 12. Simulated cutting forces for  $v_c = 318$  m/min and  $h = 0.2$  mm. Different  $\mu$  values are implemented in the friction modeling, and the results with/without the limitation of local shear flow stress are compared. The straight solid line indicates the experimental cutting force level, while the dashed line corresponds to the feed force result from the experiment.

#### 4.1.3. Simulated process forces

The simulated cutting force  $F_c$  and feed force  $F_f$  demonstrate similar patterns of variation as the friction coefficient  $\mu$  changes. In

general, there appears to be a synchronous relationship between the contact length and the feed force as well, as both variables show similar variations with changes in  $\mu$  in Figs. 8 and 12. However, the trend that the numerical model underestimates the feed force  $F_f$  without largely overestimating the cutting force  $F_c$  is observed in Fig. 12 in all cases. The similar relative errors in averaged cutting and feed forces across different friction conditions in Fig. 13 further support this finding. When the frictional stress is not limited by the shear flow stress, both the cutting and feed forces initially increase with higher values of  $\mu$ . As  $\mu$  surpasses 0.35, the cutting force levels off, whereas the feed force keeps growing until  $\mu$  reaches 0.55, after which it stagnates. This value of 0.55 for  $\mu$  marks a turning point for the growth rate of contact length as well, as shown in Fig. 8. On the other hand, when the frictional stress is limited by the shear flow stress, the simulated forces tend to be smaller compared to the results without this limitation, as the flow rule exerts a certain degree of control over the chip's sliding at the tool surface.

The force results for the specified process parameters listed in Table 6 are further depicted in Fig. 13. The simulation is able to capture the overall trend when the changing process parameters, i.e. the cutting speed and feed, are varied. As anticipated, accurately predicting the feed force  $F_f$  comes at the expense of compromising the accuracy of the cutting force  $F_c$  prediction. The force results given  $\mu = 0$  roughly demonstrate how much extra energy during the machining is required due to friction. To evaluate the suitability of using an apparent COF obtained from experiments in numerical simulations, the values of  $\mu_{app}$  are calculated using Eq. (11) and presented in Table 7. It is observed that the shear flow stress limit does not affect the outcome when

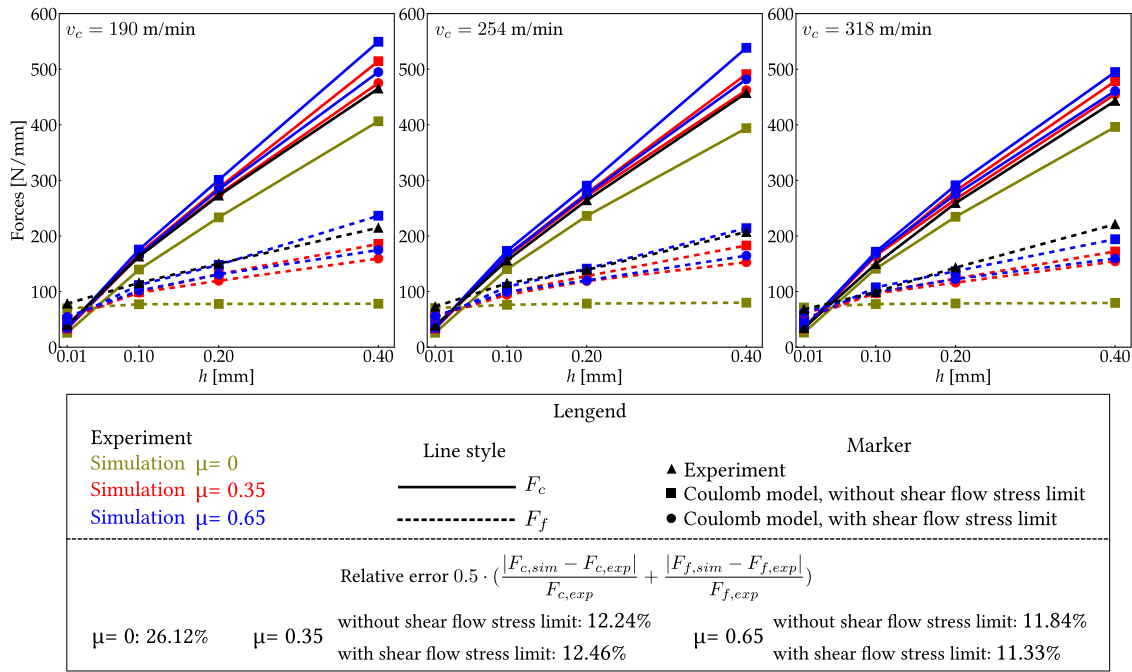


Fig. 13. Comparison between simulated and experimental cutting forces with different  $v_c$  and  $h$ . Different  $\mu$  values are implemented in the Coulomb friction model. The formula for calculating the relative error is provided, and the error values listed are the averaged results across all the tested cutting parameters.

Table 7  
Comparison of  $\mu_{app}$  between experimental and simulated results.

| $v_c$ [m/min] | Experiment $\mu_{app}$ | Simulation $\mu_{app}$ |                    |                       |                    |                       |                    |
|---------------|------------------------|------------------------|--------------------|-----------------------|--------------------|-----------------------|--------------------|
|               |                        | $\mu = 0$              |                    | $\mu = 0.35$          |                    | $\mu = 0.65$          |                    |
|               |                        | No shear stress limit  | Shear stress limit | No shear stress limit | Shear stress limit | No shear stress limit | Shear stress limit |
| 190           | 0.33                   | 0.00                   | 0.25               | 0.25                  | 0.34               | 0.34                  |                    |
| 254           | 0.31                   | 0.01                   | 0.26               | 0.26                  | 0.29               | 0.29                  |                    |
| 318           | 0.42                   | 0.01                   | 0.24               | 0.24                  | 0.27               | 0.27                  |                    |

implementing the Coulomb friction model. However, the simulated  $\mu_{app}$  value is consistently lower than the implemented  $\mu$ . This suggests that relying on such an apparent COF from experiments may not yield the expected level of friction in simulations and does not accurately represent the true physical conditions at the tool-chip contact. Although an inverse method can be used to identify a suitable value of  $\mu$  for accurately predicting the feed force  $F_f$ , this approach may result in an overestimation of the cutting force  $F_c$ .

#### 4.2. Physical parameter dependent friction modeling and chip formation behaviors

Fig. 14 presents the predicted contact states when the physical parameter dependent friction models listed in Table 4 are implemented in the simulation. The frictional stress in this case is not limited by the shear flow stress. Firstly, the results of  $T$ -dependent friction models are examined. Model 1 behaves as if it is a constant COF value of 0.5 being applied at the contact, while Model 2 seems to produce a result similar to a smaller  $\mu$  with limited local variation. Consequently, the differences in simulated contact lengths and sliding speed profiles follow the pattern discussed in Section 4.1. When comparing the outcomes of Models 3 and 4, despite their similar total contact lengths, the discrepancy in  $v_{rel}$  confirms that higher friction at the end of the contact on the rake face leads to relatively slower sliding around the cutting edge. Overall, the findings from temperature-dependent friction modeling indicate that the involvement of temperature in friction modeling may not show distinct effect. This can be attributed to the relatively uniform temperature distribution observed in the contact region and the limited

sensitivity of the friction models to temperature changes. However, developing friction models that exhibit even stronger sensitivity to temperature lacks a solid physical basis. Comparing Models 5 and 6 clarifies the impact of  $v_{rel}$  on the COF. Model 5, with a higher COF around the cutting edge, does not result in a significant expansion of the contact length. The large contact pressure  $\sigma_n$ , which is over 2.4 GPa around the cutting edge region, is primarily due to the large local friction. In contrast, Model 6, where a higher COF is assigned at the end of the tool-chip contact region, leads to a larger simulated contact length. Although the contact pressure around the cutting edge is smaller compared to that in the result with Model 5, the equivalent plastic strain field in Fig. 15 shows a thicker sheared layer in the second deformation zone, supporting the idea that friction at the end part of the tool-chip contact has a more pronounced influence on the contact length and the material deformation of the chip's contact side. The  $\sigma_n$ -dependent friction models (Models 7 and 8) exhibit similar trends to Models 5 and 6 and will not be further elaborated. In summary, the length of the contact region is primarily influenced by the friction at the end of the contact region. While the material's flowability around the cutting edge and the normal pressure are also likely to be influenced by the local friction, the friction at the end of the tool-chip contact region has a more significant impact on the chip formation process.

When using Model 1 and Model 5 obtained from the calibration work in the literature, the assigned value of  $\mu$  remains relatively constant throughout the entire contact region. The effect of physical parameters dependent friction models on the simulation outcomes is not discernible compared to simply using a constant COF value. In addition to the differences in the contact states discussed in Section 1, it is

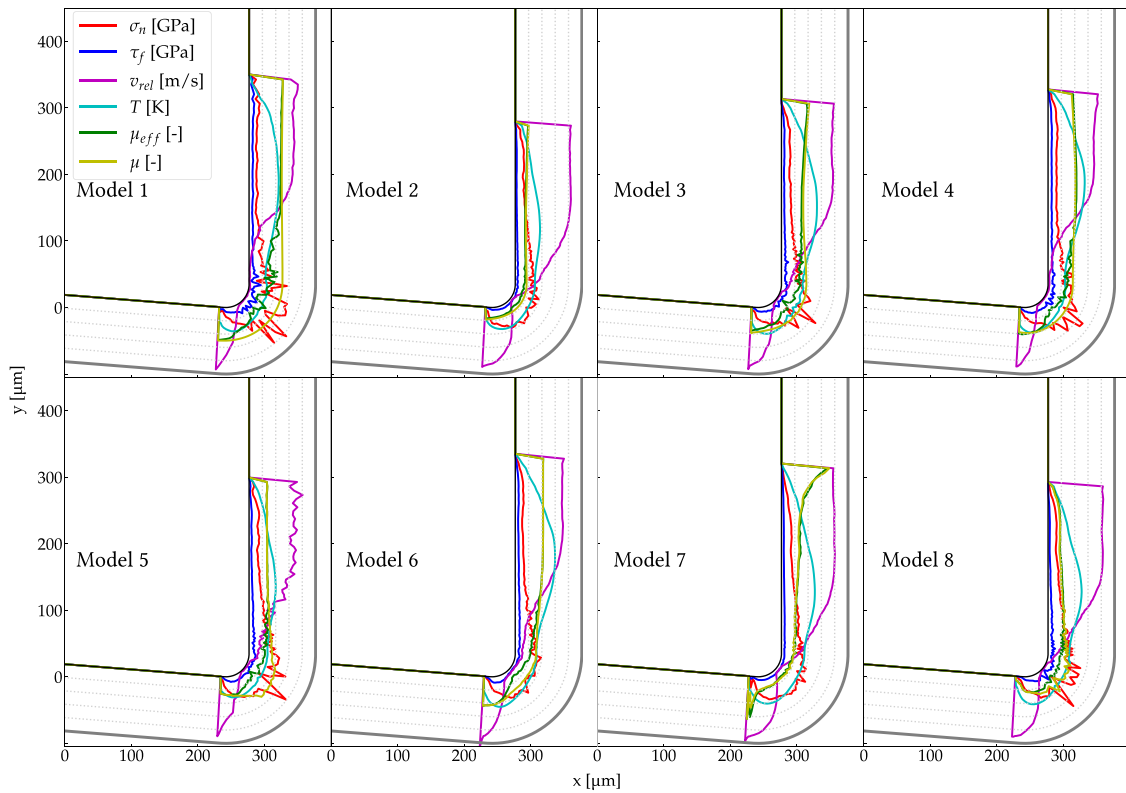


Fig. 14. Distribution of variables including  $\sigma_n$ ,  $\tau_f$ ,  $v_{rel}$ ,  $T$ ,  $\mu_{eff}$  and assigned  $\mu$  at the contact region when physical parameter dependent friction models in Table 4 are implemented in the simulation. The profiles of  $\mu$  indicate the assigned COF value locally at the contact.  $v_c = 318$  m/min,  $h = 0.2$  mm. While the tool surface indicates zeros for  $\sigma_n$ ,  $\tau_f$ ,  $v_{rel}$ ,  $\mu_{eff}$  and  $\mu$ , and 900 K for  $T$ . The outer solid gray line represents the maximum scale of each variable:  $\sigma_n$ ,  $\tau_f = 4$  GPa,  $v_{rel} = 6$  m/s,  $T = 1500$  K and  $\mu_{eff}$ ,  $\mu = 1$ .

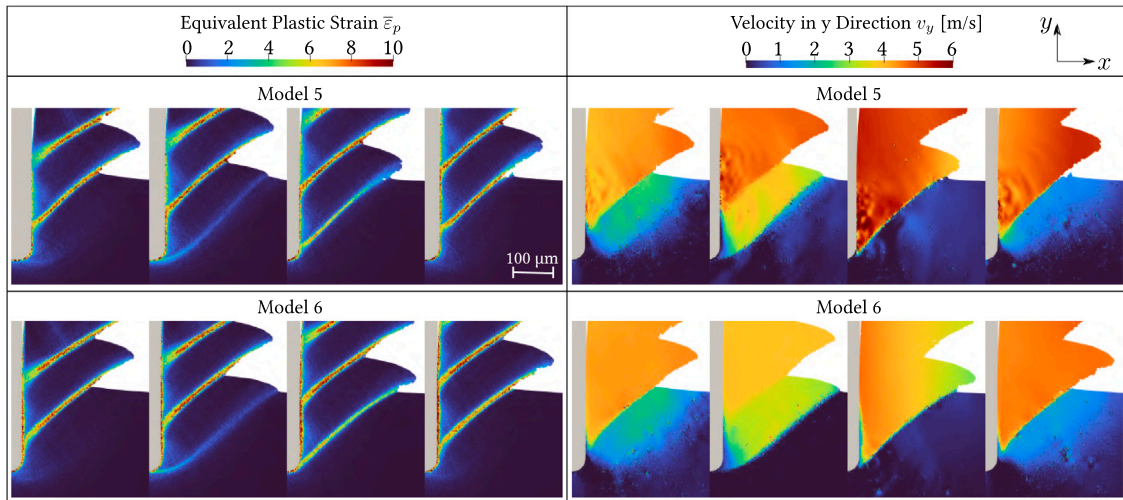
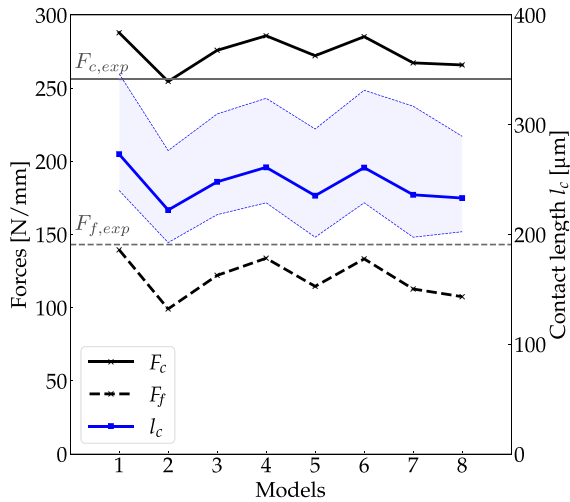


Fig. 15. Simulated equivalent plastic strain  $\bar{\epsilon}_p$  and velocity field in  $y$  direction when physical parameter dependent friction models 5 and 6 in Table 4 are implemented.  $v_c = 318$  m/min,  $h = 0.2$  mm. The four clips demonstrate the sequential stages of a segment formation.

crucial to consider the valid range of models when using experimentally calibrated ones in cutting simulations, particularly those dependent on  $v_{rel}$ . As the sliding friction may not be consistently present across the entire contact region between the tool and chip, the assigned  $\mu$  value can exceed the calibrated range of the model, resulting in the model itself meaningless.

Fig. 16 displays the process forces and contact lengths obtained from physical parameter dependent friction models. The simulated feed force consistently falls below the experimental value, no matter which

specific friction model is used. Furthermore, there is a simultaneous variation between the cutting and feed forces, regardless of the particular physical contact variables incorporated in each model. This again raises the question of whether trying to remedy the underestimated feed force in simulations by solely depending on the friction model is effective, especially when the cutting force is correctly predicted. Once more, a close correlation is observed between the force and contact length values, further suggesting a potential interdependence between these two factors in the cutting process.



**Fig. 16.** Simulated process forces and contact lengths using physical parameter dependent friction models in Table 4. The solid horizontal line indicates the experimental cutting force  $F_{c,exp}$ , while the dashed horizontal line represents the level of the experimental feed force  $F_{f,exp}$ . The major contact length that contributes to a wear mark on the rake face from the cutting experiment is  $337 \mu\text{m}$  and can be referred to Fig. 5.

#### 4.3. Discussion

Based on the aforementioned results, some key points emphasizing the nature and uncertainties involved in friction modeling and model identification for machining processes can be summarized as follows:

- Friction modeling and contact states

From a modeling perspective, it becomes evident that the friction occurring at the end of the tool-chip contact demands substantial attention due to its profound influence on the degree of hardening on the chip's contact side, the contact length, and the resulting process forces. Additionally, the formation of the plastic contact zone, including the sticking region, is primarily determined by the frictional stress at the end of the tool-chip contact, where the sliding behavior typically presents. In the sliding region, the friction remains within the sliding friction regime, whereas in the sticking region, the concept of sliding friction is no longer valid. Moreover, in the elastic contact region, the effective COF can closely follow the originally assigned value. However, in the plastic contact region, the effective COF may deviate from the initially specified value. The interplay of these factors, along with the dynamic variation of contact states during segmented chip formation, introduces uncertainties in the identification of models, particularly those that rely on local physical variables at the contact interface.

- Frictional stress limited by shear flow stresses

Arrazola et al. [44] have argued against limiting the shear stress for friction modeling in FEM cutting simulations, stating that it lacks practical justification, and the use of stick-slip friction models in machining simulations should be approached with caution. The outcomes of the current study also questions the validity of limiting the frictional stress by the shear flow stress of the local material, as this approach is unable to accurately capture the existence of a sticking region on the rake face. As the sticking phenomenon observed around the cutting edge and on the rake face is a consequence of the cutting process, imposing an artificial limit on the frictional stress using the local shear flow stress violates the cause-and-effect relationship. As the normal stress at the interface increases from the end of the contact towards the cutting edge, the frictional stress also increases. This increase in frictional stress

eventually reaches a threshold where the relative sliding speed starts to decrease. The velocity of the chip material at the contact is slower than that inside the chip, leading to a deformation gradient and material hardening. When the sliding speed reduces to zero, the local chip material ceases relative movement on the rake face. With the prerequisite that the frictional stress cannot reverse the sliding direction, the chip material at the contact maintains its relative position on the tool surface and forms a so-called sticking zone, and a transition from sliding friction to static friction is achieved. This indicates that the presence of the sticking zone does not necessarily result from high local frictional stress. On the other hand, limiting the frictional stress by shear flow stress in simulation fails to generate sufficient deformation gradient along the direction perpendicular to the rake face, and thus no sticking phenomenon occurs. Furthermore, as mentioned in Section 1, some studies have attempted to artificially divide the rake face into sliding and sticking regions and assign different friction laws to each region. This approach is rather complicated, as determining the contact length and the sticking zone is not straightforward. More importantly, adopting such an approach is inherently illogical because the formation of the sticking zone arises as a consequence of the interaction between the tool and workpiece in the simulation, and it should not be treated as an input for numerical models.

- Possible reasons for the underestimation of feed forces

Increasing the friction in simulation does lead to higher cutting and feed forces. However, it is important to note that there are limits to how much the forces can be increased. Adjusting the friction models alone cannot fully compensate for the deviation in the predicted feed force in the simulation. Besides, the feed force cannot be increased independently without a corresponding increase in the cutting force. Hence, it is necessary to consider additional factors in order to address the issue of under-predicted feed force:

1. Geometry of cutting edge

On the one hand, the simulation employs a simplified representation of the cutting edge as a tangential arc to the rake and clearance faces. It is important to note that this smooth arc may not accurately reflect the real micro geometry of the cutting edge, as it can vary depending on the method used for cutting edge preparation [88]. On the other hand, during the initial stages of the high speed machining, the cutting edge experiences rapid deformation and wear. This phenomenon was observed in machining experiments involving AISI 304 steel conducted by Laakso et al. [89]. The authors also performed FEM machining simulations and modeled the cutting tool as an elastoplastic material. The resulting plastic deformation at the cutting edge contributes to an approximately 20% increase in the feed force after 24 ms of the machining time. Indeed, the incorrect representation of the cutting edge also introduces inaccuracies in the inverse identification of the constitutive model, consequently causing discrepancies between the simulated and actual experimental force results.

2. Dynamic behavior in chip formation

During cutting experiments, the continuous or segmented chip generated can exhibit vibrational behavior on the tool surface. This chip behavior can lead to an extended region on the tool rake face where traces of the workpiece material are observed, extending beyond the primary contact area responsible for tool wear as shown in Fig. 5. The extended contact length can be intuitively associated with an increase in the feed force in experiments due to the friction on the rake face, while the cutting force remains

relatively unchanged. This could suggest why measurements obtained using “split tool” or “partially restricted contact length tool” methods, as discussed in Section 1.2.1, often reveal a COF value at the end of the contact region on the tool rake face exceeding one, as it is conceivable that these regions are within the dynamic vibrating contact area. However, numerical simulations with short cutting distances are unable to replicate these vibrating behaviors, and thus the predicted feed forces are consistently underestimated.

### 3. Continuum hypotheses

It has been reported in [86] that the hardening degree of the sheared layer at the chip’s contact side could exceed the value observed in the primary shear band. This highly distorted material may lie outside the calibrated range of the Johnson–Cook model and thus the extreme deformation cannot be fully represented. In addition, the impact of friction on the material behavior in return remains unclear, and the application of the isotropic Johnson–Cook model warrants further discussion. Laws governing other hardening behaviors in metal cutting might need to be developed and tested in simulations. Furthermore, the assumption of continuum theory in the mechanical domain may no longer be valid for the contact interface, as it may not behave as a solid state under extreme deformation conditions. Validations and investigations are needed to fully understand these complexities in the machining process.

## 5. Conclusion

This study highlights the significance of investigating how friction affects chip formation as well as process forces in numerical simulations. According to the sensitivity studies, the friction modeling in the elastic contact region, located at the end of the chip-tool interface, plays a crucial role in determining the contact length and the feed force. On the contrary, modeling friction in the plastic contact region including the sticking region appears to be less critical. The magnitude of frictional stress in the plastic contact region is influenced not only by the normal contact pressure and the prescribed coefficient of friction, but also by the sliding material in the elastic contact zone. Although the COF value might be influenced by the local physical contact states, using a constant Coulomb friction model specific to certain cutting conditions is considered an acceptable simplification. The reason is that within the elastic contact region, the variation of the physical conditions like temperature and sliding speed tends to be negligible. Given the diverse impact of friction at different locations at the tool-chip interface, the use of textured tools featuring hollow structures at distinct places on the rake face is expected to demonstrate varying levels of effectiveness in facilitating chip flow, lowering process forces and extending tool life. For relevant examples, one may refer to the work of Sugihara et al. [90]. In return, properly designed textured tools could also theoretically be utilized to assess the local COF value at the end of the tool-chip contact region without substantially changing the stress distribution.

Regarding the available friction models, when employing experimentally calibrated ones in numerical simulations, whether they are constant Coulomb models estimated using the Albrecht law or physically parameter dependent models, it is crucial to exercise caution. Replicating exact tribological conditions in the machining process poses challenges for current experimental methods. Moreover, due to the presence of the static friction, it is impossible to exert the prescribed frictional stresses in the sticking region, which suggests the inversely calibrated friction model through simulation may also lose their rationality. Importantly, imposing a limitation on friction based on shear flow stress in numerical simulations is not a justifiable approach.

Considering the ease of controlling the process parameters in comparison to physical contact parameters during experiments, and the correlation between the cutting parameters and the physical contact conditions as well as the material hardening states in the chip, it may be more practical to calibrate a phenomenological friction model based on the cutting parameters directly from machining experiments. The friction model thus shifts from  $\mu \sim \mu(\sigma_n, v_{rel}, T, \dots)$  to  $\mu \sim \mu(v_c, h, \dots)$ . Such an adapted friction model holds potential advantages for both analytical and numerical modeling methods of the cutting process. Importantly, the calibrated model has limited applicability primarily to the respective cutting processes.

In cutting simulations, increasing the friction does not indefinitely lead to higher predicted process forces. The insufficient feed force predicted by numerical simulations should not be solely linked to friction modeling. Other factors, such as the cutting edge geometry, the dynamics of chip sliding, and the material’s flow behavior to friction, should also be considered. Also, owing to the extremely large hardening in the sheared layer of chip’s contact side, the capabilities of the current continuum modeling approach based on the Johnson–Cook hardening law is questioned. Enhancements such as incorporating more sophisticated hardening laws and studying the friction impact on material behaviors might be necessary.

Several aspects can be considered for the future work. Given the possibly different contact conditions on the clearance face in contrast to that on the rake face, it is crucial to conduct a comprehensive exploration of friction modeling on the clearance face as well, especially under the condition where the flank wear land forms during the cutting process. Additionally, a study of the relationship between friction and worn tool geometries might also be worth considering.

### CRediT authorship contribution statement

**Nanyuan Zhang:** Writing – original draft, Software, Methodology, Investigation, Conceptualization. **Hagen Klippel:** Writing – review & editing, Software, Methodology. **Fabian Kneubühler:** Writing – review & editing, Methodology, Investigation. **Mohamadreza Afrasiabi:** Writing – review & editing, Software, Methodology. **Michal Kuffa:** Writing – review & editing, Supervision. **Konrad Wegener:** Writing – review & editing, Supervision.

### Declaration of competing interest

The authors declare that they have no known competing financial interests or personal relationships that could have appeared to influence the work reported in this paper.

### Data availability

Data will be made available on request.

### Declaration of Generative AI and AI-assisted technologies in the writing process

During the preparation of this work the author(s) used ChatGPT in order to improve language. After using this tool/service, the authors reviewed and edited the content as needed and take full responsibility for the content of the publication.

### Acknowledgment

The authors gratefully acknowledge ScopeM of ETH Zürich for their assistance with the SEM analysis of the cutting tools.

**Appendix. Stabilizers used in SPH discretization**

The resulting formulations for the momentum equation and the position-speed relation with stabilizers are presented as

$$\langle \dot{v}_i \rangle = \sum_j \left( \frac{\bar{\sigma}_{ij}}{\rho_i^2} + \frac{\bar{\sigma}_{ij}}{\rho_j^2} + \underbrace{\Pi_{ij} \underline{I}}_{a.v.} + \underbrace{(\underline{\Theta}_{ij} + \underline{\Theta}_{ji})}_{a.s.} f^{as n^{as}} \right) \cdot \nabla W_{ij} m_j + \frac{b_i}{m_i}, \quad (A.1)$$

and

$$\langle \dot{x}_i \rangle = v_i + e^{XSPH} \underbrace{\sum_j \frac{m_j}{\rho_i + \rho_j} (v_j - v_i) W_{ij}}_{XSPH \text{ correction}}. \quad (A.2)$$

The artificial viscosity in Eq. (A.1) is given by:

$$\Pi_{ij} \underline{I} = \begin{cases} \frac{-\alpha^{av} \bar{c}_{ij} \mu_{ij} + \beta^{av} \mu_{ij}^2}{\bar{\rho}_{ij}} \underline{I}, & v_{ij} \cdot x_{ij} < 0, \\ 0, & v_{ij} \cdot x_{ij} \geq 0 \end{cases}, \quad (A.3)$$

with

$$\mu_{ij} = \frac{\bar{h}_{s,ij} v_{ij} \cdot x_{ij}}{|x_{ij}|^2 + \epsilon^{av} \bar{h}_{s,ij}^2}, \quad (A.4)$$

where  $\alpha^{av}$ ,  $\beta^{av}$  and  $\epsilon^{av}$  are parameters for artificial viscosity and defined as 1.0, 1.0 and 0.1 respectively in this study.  $c$  is the speed of sound given by  $c = \sqrt{K/\rho}$ . Variables represented with an overbar and an subscript  $ij$  signify the averaged values, for example,  $\bar{c}_{ij} = 0.5 * (c_i + c_j)$ . Otherwise, the subscript  $ij$  alone denotes the difference of the variable, such as  $x_{ij} = x_i - x_j$ .

The introduction of artificial stress serves the purpose of generating repulsive stresses when particles tend to cluster. The computation of artificial stress involves a relatively intricate procedure. Initially, the Cauchy stress tensor is diagonalized:

$$\bar{\underline{\sigma}} = \underline{R} \underline{\sigma} \underline{R}^T, \quad (A.5)$$

where  $\underline{R}$  is the rotation matrix. With the index notation, the diagonalized artificial stress tensor  $\bar{\underline{\Theta}}$  is calculated by:

$$\bar{\Theta}_{kk} = \begin{cases} -\epsilon^{as} \frac{\bar{\sigma}_{kk}}{\rho^2}, & \bar{\sigma}_{kk} > 0, \\ 0, & \bar{\sigma}_{kk} \leq 0. \end{cases} \quad (A.6)$$

$\epsilon^{as}$  is a coefficient which controls the magnitude of the repulsive stress and set as 0.3 in the study. The artificial stress matrix is finally given by rotating the  $\bar{\underline{\Theta}}$  matrix back

$$\underline{\underline{\Theta}} = \underline{R}^T \bar{\underline{\Theta}} \underline{R}. \quad (A.7)$$

Furthermore, the term  $f^{as}$  roughly represents the scale how close the particles cluster and is determined by

$$f^{as} = \frac{W_{ij}}{W_0}, \quad (A.8)$$

where  $W_0$  is the kernel function given the initial particle spacing  $\Delta x$ . Besides,  $n^{as}$  is an exponential parameter in the artificial stress term that further regulates the magnitude of the repulsive stress. This parameter is set as 4 in the simulation.

Regarding the XSPH stabilizer, it can be understood as the velocity of each particle being averaged by its neighboring particles. Typically,  $e^{XSPH}$  falls within the range of 0 to 1, and it governs the extent of the averaging effect. In this study, this parameter is set with a value of 0.5.

**References**

[1] Arrazola P, Özel T, Umbrello D, Davies M, Jawahir I. Recent advances in modelling of metal machining processes. *CIRP Ann.* 2013;62(2):695–718.

[2] Melkote SN, Grzesik W, Outeiro J, Rech J, Schulze V, Attia H, Arrazola P-J, M'Saoubi R, Saldana C. Advances in material and friction data for modelling of metal machining. *CIRP Ann.* 2017;66(2):731–54.

[3] Lorentzon J, Järnström N. Modelling tool wear in cemented-carbide machining alloy 718. *Int J Mach Tools Manuf* 2008;48(10):1072–80.

[4] Laakso SV, Agmell M, Ståhl J-E. The mystery of missing feed force—The effect of friction models, flank wear and ploughing on feed force in metal cutting simulations. *J Manuf Process* 2018;33:268–77.

[5] Haglund A, Kishawy H, Rogers R. An exploration of friction models for the chip–tool interface using an Arbitrary Lagrangian–Eulerian finite element model. *Wear* 2008;265(3–4):452–60.

[6] Zorev N. Inter-relationship between shear processes occurring along tool face and shear plane in metal cutting. *Int. Res. Prod. Eng.* 1963;49:143–52.

[7] Liang X, Liu Z, Wang B, Chunjin W, Cheung B. Friction behaviors in the metal cutting process: state of the art and future perspectives. *Int. J. Extreme Manuf.* 2022.

[8] Zemzemi F, Rech J, Salem WB, Dogui A, Kapsa P. Identification of a friction model at tool/chip/workpiece interfaces in dry machining of AISI4142 treated steels. *J Mater Process Technol* 2009;209(8):3978–90.

[9] Rech J, Arrazola P, Claudin C, Courbon C, Pusavec F, Kopac J. Characterisation of friction and heat partition coefficients at the tool-work material interface in cutting. *CIRP Ann.* 2013;62(1):79–82.

[10] Smolenicki D, Boos J, Kuster F, Roelofs H, Wyen CF. In-process measurement of friction coefficient in orthogonal cutting. *CIRP Ann.* 2014;63(1):97–100.

[11] Denkena B, Krödel A, Beblein S. A novel approach to determine the velocity dependency of the friction behavior during machining by means of digital particle image velocimetry (DPIV). *CIRP J. Manuf. Sci. Technol.* 2021;32:81–90.

[12] Lim S, Ashby M, Brunton J. The effects of sliding conditions on the dry friction of metals. *Acta Metall.* 1989;37(3):767–72.

[13] Ozlu E, Budak E, Molinari A. Analytical and experimental investigation of rake contact and friction behavior in metal cutting. *Int. J. Mach. Tools Manuf.* 2009;49(11):865–75.

[14] Schulze V, Bleicher F, Courbon C, Gerstenmeyer M, Meier L, Philipp J, Rech J, Schneider J, Segebade E, Steininger A, Wegener K. Determination of constitutive friction laws appropriate for simulation of cutting processes. *CIRP J. Manuf. Sci. Technol.* 2022;38:139–58.

[15] Meier L, Schaal N, Wegener K. In-process measurement of the coefficient of friction on titanium. *Proc. CIRP* 2017;58:163–8.

[16] Bonnet C, Rech J, Poulachon G. Characterization of friction coefficient for simulating drilling contact for titanium TiAl6V4 alloy. *CIRP J. Manuf. Sci. Technol.* 2020;29:130–7.

[17] Egana A, Rech J, Arrazola P. Characterization of friction and heat partition coefficients during machining of a TiAl6V4 titanium alloy and a cemented carbide. *Tribol. Trans.* 2012;55(5):665–76.

[18] Brocaïl J, Watremez M, Dubar L. Identification of a friction model for modelling of orthogonal cutting. *Int. J. Mach. Tools Manuf.* 2010;50(9):807–14.

[19] Klocke F, Trauth D, Shirobokov A, Mattfeld P. FE-analysis and in situ visualization of pressure-, slip-rate-, and temperature-dependent coefficients of friction for advanced sheet metal forming: development of a novel coupled user subroutine for shell and continuum discretization. *Int. J. Adv. Manuf. Technol.* 2015;81:397–410.

[20] Moufki A, Molinari A, Dudzinski D. Modelling of orthogonal cutting with a temperature dependent friction law. *J. Mech. Phys. Solids* 1998;46(10):2103–38.

[21] Molinari A, Moufki A. A new thermomechanical model of cutting applied to turning operations. Part I. Theory. *Int. J. Mach. Tools Manuf.* 2005;45(2):166–80.

[22] Puls H, Klocke F, Lung D. Experimental investigation on friction under metal cutting conditions. *Wear* 2014;310(1–2):63–71.

[23] Johnson GR. A Constitutive Model and Data for Metals Subject to Large Strains, High Strain Rate and High Temperatures. In: *Proc. of 7th int. symp. on ballistics, the Hague.* 1983.

[24] Peng B, Bergs T, Klocke F, Döbbeler B. An advanced FE-modeling approach to improve the prediction in machining difficult-to-cut material. *Int J Adv Manuf Technol* 2019;103(5):2183–96.

[25] Afrasiabi M, Meier L, Röthlin M, Klippel H, Wegener K. GPU-accelerated meshfree simulations for parameter identification of a friction model in metal machining. *Int J Mech Sci* 2020;176:105571.

[26] Segebade E, Schneider J, Schulze V. Tribological effects in and by metal cutting. In: *Key Engineering Materials*, vol. 767, Trans Tech Publ; 2018, p. 3–24.

[27] Storchak M, Möhring H-C, Stehle T. Improving the friction model for the simulation of cutting processes. *Tribol Int* 2022;167:107376.

[28] Merchant ME. Mechanics of the metal cutting process. I. Orthogonal cutting and a type 2 chip. *J. Appl. Phys.* 1945;16(5):267–75.

[29] Albrecht P. New developments in the theory of the metal-cutting process: part I. The ploughing process in metal cutting. *J. Eng. Ind.* 1960;82(4):348–57.

[30] Wyen C-F, Wegener K. Influence of cutting edge radius on cutting forces in machining titanium. *CIRP Ann.* 2010;59(1):93–6.

[31] Arrazola P, Ugarte D, Dominguez X. A new approach for the friction identification during machining through the use of finite element modeling. *Int. J. Mach. Tools Manuf.* 2008;48(2):173–83.

- [32] Kato S, Yamaguchi K, Yamada M. Stress Distribution at the Interface Between Tool and Chip in Machining. *J. Eng. Ind.* 1972;94(2):683–9. <http://dx.doi.org/10.1115/1.3428229>.
- [33] Childs T. Friction modelling in metal cutting. *Wear* 2006;260(3):310–8.
- [34] Maekawa K, Kitagawa T, Childs T. Friction characteristics at tool-chip interface in steel machining. In: *Tribology Series*, vol. 32, Elsevier; 1997, p. 559–67.
- [35] Ortiz-de Zarate G, Madariaga A, Arrazola PJ, Childs TH. A novel methodology to characterize tool-chip contact in metal cutting using partially restricted contact length tools. *CIRP Ann.* 2021;70(1):61–4.
- [36] Bonnet C, Valiorgue F, Rech J, Claudin C, Hamdi H, Bergheau J, Gilles P. Identification of a friction model—application to the context of dry cutting of an AISI 316L austenitic stainless steel with a TiN coated carbide tool. *Int J Mach Tools Manuf* 2008;48(11):1211–23.
- [37] Claudin C, Mondelin A, Rech J, Fromentin G. Effects of a straight oil on friction at the tool-workmaterial interface in machining. *Int J Mach Tools Manuf* 2010;50(8):681–8.
- [38] Puls H, Klocke F, Lung D. A new experimental methodology to analyse the friction behaviour at the tool-chip interface in metal cutting. *Prod. Eng.* 2012;6(4):349–54.
- [39] Leveille T, Fabre D, Cici M, Sijobert J, Doubenskaia M, Courbon C. Development of a novel high temperature open tribometer with laser-based heating system. *Wear* 2021;477:203881.
- [40] Olsson M, Söderberg S, Jacobson S, Hogmark S. Simulation of cutting tool wear by a modified pin-on-disc test. *Int J Mach Tools Manuf* 1989;29(3):377–90.
- [41] Özel T. The influence of friction models on finite element simulations of machining. *Int J Mach Tools Manuf* 2006;46(5):518–30.
- [42] Filice L, Micari F, Rizzuti S, Umbrello D. A critical analysis on the friction modelling in orthogonal machining. *Int J Mach Tools Manuf* 2007;47(3–4):709–14.
- [43] Iqbal SA, Mativenga P, Sheikh MA. Contact length prediction: mathematical models and effect of friction schemes on FEM simulation for conventional to HSM of AISI 1045 steel. *Int J Mach Mach Mater* 2008;3(1–2):18–33.
- [44] Arrazola PJ, et al. Investigations on the effects of friction modeling in finite element simulation of machining. *Int. J. Mech. Sci.* 2010;52(1):31–42.
- [45] Atlati S, Haddag B, Nouari M, Moufki A. Effect of the local friction and contact nature on the built-up edge formation process in machining ductile metals. *Tribol Int* 2015;90:217–27.
- [46] Franchi R, Del Prete A, Umbrello D. Inverse analysis procedure to determine flow stress and friction data for finite element modeling of machining. *Int J Mater Form* 2017;10:685–95.
- [47] Klippel H. Constitutive Equations for Simulation of Metal Cutting with Meshless Methods on GPU (Ph.D. thesis), 2021, No. 27671, ETH Zurich.
- [48] Malakizadi A, Hosseinkhani K, Mariano E, Ng E, Del Prete A, Nyborg L. Influence of friction models on FE simulation results of orthogonal cutting process. *Int J Adv Manuf Technol* 2017;88(9):3217–32.
- [49] Limido J, Espinosa C, Salaün M, Lacomme J-L. SPH method applied to high speed cutting modelling. *Int. J. Mech. Sci.* 2007;49(7):898–908.
- [50] Rabczuk T, Samaniego E. Discontinuous modelling of shear bands using adaptive meshfree methods. *Comput Methods Appl Mech Engrg* 2008;197(6–8):641–58.
- [51] Calamaz M, Limido J, Nouari M, Espinosa C, Coupard D, Salaün M, Girof F, Chieragatti R. Toward a better understanding of tool wear effect through a comparison between experiments and SPH numerical modelling of machining hard materials. *Int. J. Refract. Met. Hard Mater.* 2009;27(3):595–604.
- [52] Eberhard P, Gaugele T. Simulation of cutting processes using mesh-free Lagrangian particle methods. *Comput Mech* 2013;51:261–78.
- [53] Tan Y, Yang D, Sheng Y. Study of polycrystalline Al<sub>2</sub>O<sub>3</sub> machining cracks using discrete element method. *Int J Mach Tools Manuf* 2008;48(9):975–82.
- [54] Uhlmann E, Gerstenberger R, Kuhnert J. Cutting simulation with the meshfree finite pointset method. *Proc. CIRP* 2013;8:391–6.
- [55] Rodríguez JM, Carbonell JM, Cante J, Oliver J. Continuous chip formation in metal cutting processes using the Particle Finite Element Method (PFEM). *Int J Solids Struct* 2017;120:81–102.
- [56] Kahwash F, Shyha I, Maheri A. Dynamic simulation of machining composites using the explicit element-free Galerkin method. *Compos. Struct.* 2018;198:156–73.
- [57] Więckowski Z. The material point method in large strain engineering problems. *Comput Methods Appl Mech Engrg* 2004;193(39–41):4417–38.
- [58] Gu X, Dong C, Cheng T. MPM simulations of high-speed machining of Ti6Al4V titanium alloy considering dynamic recrystallization phenomenon and thermal conductivity. *Appl Math Model* 2018;56:517–38.
- [59] Illoul L, Lorong P. On some aspects of the CNEM implementation in 3D in order to simulate high speed machining or shearing. *Comput Struct* 2011;89(11–12):940–58.
- [60] Markopoulos AP, Karkalos NE, Papazoglou E-L. Meshless methods for the simulation of machining and micro-machining: a review. *Arch Comput Methods Eng* 2020;27(3):831–53.
- [61] Harzallah M, Pottier T, Gilblas R, Landon Y, Mousseigne M, Senatore J. Thermo-mechanical coupling investigation in Ti-6Al-4V orthogonal cutting: Experimental and numerical confrontation. *Int J Mech Sci* 2020;169:105322.
- [62] Röthlin M, Klippel H, Afrasiabi M, Wegener K. Metal cutting simulations using smoothed particle hydrodynamics on the GPU. *Int J Adv Manuf Technol* 2019;102(9):3445–57.
- [63] Zhang N, Klippel H, Afrasiabi M, Röthlin M, Kuffa M, Bambach M, Wegener K. Hybrid SPH-FEM solver for metal cutting simulations on the GPU including thermal contact modeling. *CIRP J. Manuf. Sci. Technol.* 2023;41:311–27.
- [64] Zhang N, Klippel H, Kneubühler F, Afrasiabi M, Röthlin M, Kuffa M, Bambach M, Wegener K. Study on the effect of wear models in tool wear simulation using hybrid SPH-FEM method. *Proc. CIRP* 2023;117:414–9.
- [65] Hajmohammadi MS, Movahhedy MR. Investigation of thermal effects on machining chatter using FEM simulation of chip formation. *Proc. CIRP* 2012;1:50–5.
- [66] Röthlin M. Meshless software tool to simulate metal cutting operations by employing contemporary numerical methods. 2019, No. 25679, ETH Zurich.
- [67] Taylor GI, Quinney H. The latent energy remaining in a metal after cold working. *Proc. R. Soc. Lond. Ser. A* 1934;143(849):307–26.
- [68] Wilkins ML. Calculation of Elastic-Plastic Flow: Technical Report. California University. Livermore Radiation Lab; 1963.
- [69] Wriggers P, Laursen TA. *Computational Contact Mechanics*, vol. 2, Springer; 2006.
- [70] Courbon C, Mabrouki T, Rech J, Mazuyer D, D'Eramo E. On the existence of a thermal contact resistance at the tool-chip interface in dry cutting of AISI 1045: Formation mechanisms and influence on the cutting process. *Appl Therm Eng* 2013;50(1):1311–25.
- [71] Haddag B, Atlati S, Nouari M, Zenasni M. Analysis of the heat transfer at the tool-workpiece interface in machining: determination of heat generation and heat transfer coefficients. *Heat Mass Transf.* 2015;51(10):1355–70.
- [72] Atlati S, Haddag B, Nouari M, Zenasni M. Thermomechanical modelling of the tool-workmaterial interface in machining and its implementation using the ABAQUS VUINTER subroutine. *Int J Mech Sci* 2014;87:102–17.
- [73] Price DJ. Smoothed particle hydrodynamics and magnetohydrodynamics. *J Comput Phys* 2012;231(3):759–94.
- [74] Monaghan J. Smoothed particle hydrodynamics. *Rep Progr Phys* 2005;68(8):1703–59.
- [75] Cummins SJ, Rudman M. An SPH projection method. *J Comput Phys* 1999;152(2):584–607.
- [76] Brookshaw L. A method of calculating radiative heat diffusion in particle simulations. *Publ Astron Soc Aust* 1985;6(2):207–10.
- [77] Eldredge JD, Leonard A, Colonius T. A general deterministic treatment of derivatives in particle methods. *J Comput Phys* 2002;180(2):686–709.
- [78] Monaghan JJ, Gingold RA. Shock simulation by the particle method SPH. *J Comput Phys* 1983;52(2):374–89.
- [79] Gray JP, Monaghan JJ, Swift R. SPH elastic dynamics. *Comput Methods Appl Mech Engrg* 2001;190(49–50):6641–62.
- [80] Monaghan J. On the problem of penetration in particle methods. *J Comput Phys* 1989;82(1):1–15.
- [81] Swegle J, Hicks D, Attaway S. Smoothed Particle Hydrodynamics Stability Analysis. *J. Comput. Phys.* 1995;116(1):123–34. <http://dx.doi.org/10.1006/jcph.1995.1010>.
- [82] Rabczuk T, Belytschko T. A three-dimensional large deformation meshfree method for arbitrary evolving cracks. *Comput Methods Appl Mech Engrg* 2007;196(29–30):2777–99.
- [83] Nianfei G, Guangyao L, Shuyao L. 3D adaptive RKPM method for contact problems with elastic-plastic dynamic large deformation. *Eng. Anal. Bound. Elem.* 2009;33(10):1211–22.
- [84] Hallquist JO, et al. *LS-DYNA theory manual*. Livermore Softw. Technol. Corp. 2006;3:25–31.
- [85] Afrasiabi M, Saelzer J, Berger S, Iovkov I, Klippel H, Röthlin M, Zabel A, Biermann D, Wegener K. A numerical-experimental study on orthogonal cutting of AISI 1045 steel and Ti6Al4V alloy: SPH and FEM modeling with newly identified friction coefficients. *Metals* 2021;11(11):1683.
- [86] Klippel H, Süßmaier S, Kuffa M, Wegener K. Dry cutting experiments database Ti6Al4V and Ck45. 2022.
- [87] Guo B, Jiang F, Yan L, Wang N, Huang H, Wang F, Xie H. Research on the analytical modeling of critical conditions of serrated chip formation based on thermal-mechanical coupled material behavior. *J. Manuf. Process.* 2021;68:71–84.
- [88] Denkena B, Biermann D. Cutting edge geometries. *CIRP Ann.* 2014;63(2):631–53.
- [89] Laakso SV, Zhao T, Agmell M, Hrechuk A, Ståhl J-E. Too sharp for its own good—Tool edge deformation mechanisms in the initial stages of metal cutting. *Proc. Manuf.* 2017;11:449–56.
- [90] Sugihara T, Kobayashi R, Enomoto T. Direct observations of tribological behavior in cutting with textured cutting tools. *Int. J. Mach. Tools Manuf.* 2021;168:103726.